J. Fluid Mech. (2003), *vol.* 492, *pp.* 147–180.
DOI: 10.1017/S0022112003005512 Printed in the United Kingdom

From spheres to circular cylinders: the stability and flow structures of bluff ring wakes

By G. J. SHEARD, M. C. THOMPSON AND K. HOURIGAN

Fluids Laboratory for Aeronautical and Industrial Research (FLAIR), Department of Mechanical Engineering, Monash University, Melbourne, Victoria 3800, Australia

(Received 18 July 2002 and in revised form 23 April 2003)

The low-Reynolds-number wake dynamics and stability of the flow past toroids placed normal to the flow direction are studied numerically. This bluff body has the attractive feature of behaving like the sphere at small aspect ratios, and locally like the straight circular cylinder at large aspect ratios. Importantly, the geometry of the ring is described by a single parameter, the aspect ratio (Ar), defined as a ratio of the torus diameter to the cross-sectional diameter of the ring. A rich diversity of wake topologies and flow transitions can therefore be investigated by varying the aspect ratio. Studying this geometry allows our understanding to be developed as to why the wake transitions leading to turbulence for the sphere and circular cylinder differ so greatly. Strouhal–Reynolds-number profiles are determined for a range of ring aspect ratios, as are critical Reynolds numbers for the onset of flow separation, unsteady flow and asymmetry. Results are compared with experimental findings from the literature. Calculated Strouhal–Reynolds-number profiles show that ring wakes shed at frequencies progressively closer to that of the straight circular cylinder wake as aspect ratio is increased from $Ar = 3$. For $Ar > 8$, the initial asymmetric transition is structurally analogous to the mode A transition for the circular cylinder, with a discontinuity present in the Strouhal–Reynolds-number profile. The present numerical study reveals a shedding-frequency decrease with decreasing aspect ratio for ring wakes, and an increase in the critical Reynolds numbers for flow separation and the unsteady flow transition. A Floquet stability analysis has revealed the existence of three modes of asymmetric vortex shedding in the wake of larger rings. Two of these modes are analogous to mode A and mode B of the circular cylinder wake, and the third mode, mode C, is analogous to the intermediate wavelength mode found in the wake of square section cylinders and circular cylinder wakes perturbed by a tripwire. Furthermore, three distinct asymmetric transition modes have been identified in the wake of small aspect ratio bluff rings. Fully developed asymmetric simulations have verified the unsteady transition for rings that exhibit a steady asymmetric wake.

1. Introduction

Wake flows of two-dimensional bluff-body geometries, and the inherent transitions with increasing Reynolds number from steady two-dimensional wake flow, through unsteady and three-dimensional flows, to fully turbulent wakes have been of interest to researchers for many decades. A recent comprehensive review of the work on the circular cylinder wake has been provided by Williamson (1996). The wake transitions for another widely studied bluff body, the sphere, are markedly different (e.g. Johnson & Patel 1999; Ormières & Provansal 1999; Tomboulides & Orszag 2000;

Thompson, Leweke & Provansal 2001*a*). There are also relevant related studies into the wakes from other body geometries such as the square cross-sectioned cylinder (e.g. Robichaux, Balachandar & Vanka 1999), and long rectangular plates (e.g. Hourigan, Thompson & Tan 2001; Mills, Sheridan & Hourigan 2002, 2003). Although these studies indicate some similarities in the bifurcations and wake dynamics from different bodies, there are also significant differences that warrant further investigation. In this paper, we are especially interested in the differences between the sphere and circular cylinder wakes which show major differences in the wake bifurcations as a function of Reynolds number. The characteristics of these geometries are now presented. The characteristics of both the mode C instability for the square cylinder and the wakes of bluff rings are also presented.

1.1. *The sphere wake*

A major difference in the wake transition behaviour of the sphere and circular cylinder wakes is that the sphere wake becomes asymmetrical prior to a transition to unsteady flow (Magarvey & Bishop 1961*a*, *b*), whereas the cylinder wake becomes unsteady before asymmetric structures become present in the wake (Williamson 1988*a*, *b*).

For the sphere wake, the transition from attached to separated flow at the rear of the sphere has been interpolated from direct numerical simulations to be $Re_{S1} = 20$ (Tomboulides, Orszag & Karniadakis 1993; Johnson & Patel 1999; Tomboulides & Orszag 2000). On increasing the Reynolds number, the wake remains steady and axisymmetric up to $Re_{S2} = 211$ (Johnson & Patel 1999). Magarvey & Bishop (1961*b*) provided early flow visualizations of a liquid sphere falling through a liquid phase. The experimental layout enabled striking images of the trailing wakes to be captured, as they were motionless in the reference frame of the camera. The transition to asymmetry is through a regular bifurcation (i.e. steady to steady flow) of the $m = 1$ azimuthal mode (Tomboulides *et al.* 1993; Tomboulides & Orszag 2000). Their studies located the transition at $Re_{S2} = 212$. In good agreement, the numerical stability analysis of Natarajan & Acrivos (1993) also found the $m = 1$ azimuthal mode to undergo a regular bifurcation at $Re_{S2} = 210$. Experiments and numerical simulations (Johnson & Patel 1999) found the resulting wake to undergo a regular bifurcation through a shift of the steady recirculating bubble behind the sphere from the axis. Two threads of vorticity trail downstream from the recirculation bubble. This wake structure has become known as the double-threaded wake, and has also been predicted numerically by Tomboulides & Orszag (2000). The beautiful early dye visualizations of Magarvey & Bishop (1961*b*) found that the double-threaded wake exists in the range $200 < Re < 350$. Since then, more accurate experiments and numerical simulations have refined this range considerably, as described below.

The steady asymmetric wake undergoes a further transition to unsteady flow at a higher Reynolds number. Through stability analysis, Natarajan & Acrivos (1993) found a time-dependent instability of the $m = 1$ azimuthal mode at $Re_{S3} = 277.5$, and the visualizations from numerical simulations (Tomboulides *et al.* 1993; Johnson & Patel 1999; Tomboulides & Orszag 2000) support this bifurcation scenario, with unsteady wakes being observed for $Re > 280$. In all instances, the unsteady wake consisted of vortex loops or hairpins shedding downstream from the sphere, in the same plane as that of the initial steady asymmetric structures. Magarvey & Bishop (1961*b*) observed this periodic wake pattern at $Re = 350$. An analysis of the transition to the periodic wake was also performed by Magarvey & MacLatchy (1965). They observed the equilibrium in transport of vorticity into and out of the near field of the double-threaded wake in the approximate range $200 < Re < 300$. For higher

Reynolds numbers, the formation of the periodic hairpin-shedding wake was required to transport the vorticity generated behind the sphere downstream. The periodic wake of the sphere remains planar-symmetric up to a Reynolds number of approximately $Re = 375$, as observed numerically by (Mittal 1999*a*, *b*). Johnson & Patel (1999) estimated the unsteady transition to occur in the range $270 < Re_{S3} < 280$.

Stability of the sphere wake has been studied using the complex wave amplitude Landau equation (Ghidersa & Dušek 2000; Thompson *et al.* 2001*a*). The coefficients of the linear and cubic terms of the Landau model were estimated from asymmetric numerical simulations close to the transition Reynolds numbers. The initial asymmetric transition was found to be a regular type transition, occurring at $Re_{S2} = 212$, and the subsequent transition was identified as being a Hopf transition at $Re_{S3} = 272$. The critical Reynolds numbers of the transitions are in agreement with previous studies. The analysis demonstrates that both transitions were shown to be supercritical (non-hysteretic).

Tomboulides *et al.* (1993) observed fine-scale flow structures in large-eddy numerical simulations in the Reynolds-number range $500 < Re < 1000$. Magarvey & Bishop (1961*b*) observed a breakdown in periodicity of the hairpin shedding for $Re > 600$ also. These results are considered to mark the onset of turbulence, and hence are beyond the scope of the present study.

1.2. *The circular cylinder wake*

The initial transition for the cylinder wake occurs with the separation of flow from the rear of the cylinder, resulting in a steady recirculation bubble. This transition was predicted by numerical stability analysis to occur at $Re_{C1} = 5$ (Noack & Eckelmann 1994*b*). The recirculation zone remains steady two-dimensional and symmetrical about the centreline of the flow until a subsequent transition to periodic flow occurs. This transition was predicted to occur at $Re_{C2} = 54$ (Noack & Eckelmann 1994*a*); however, the Galerkin method used appeared to have too few modes to capture the instability accurately. The experimentally derived results of Williamson (1988*a*, 1989) at $Re = 49$ are widely regarded as more accurate. Sheard, Thompson & Hourigan (2001) validated this finding through application of a spectral-element method, achieving $Re_{C2} = 47$, in good agreement with Dušek, Fraunié & Le Gal (1994), who obtainined a value of $Re_{C2} = 47.1$ through numerical simulation and the application of the theoretical Landau model. Dušek *et al.* (1994) identified the transition as a Hopf bifurcation.

Two three-dimensional wake states are observed in the wake behind the circular cylinder: oblique shedding and instabilities of the parallel vortex street. At Reynolds numbers $Re > 64$, oblique shedding is observed (Williamson 1988*a*, 1996), where the vortex rollers are shed at an angle to the cylinder resulting in a reduction of Strouhal number. Oblique shedding is a phenomenon associated with the interaction of nonlinear long-wavelength azimuthal modes disrupting the parallel vortex street, and as such is beyond the scope of the present work.

Experiments have found the parallel periodic vortex shedding street becomes unstable to three-dimensional instabilities at $Re > 178$ (Williamson 1988*a*, 1996). This transition was studied using a linear Floquet stability analysis (Barkley & Henderson 1996). They found that at $Re = 188.5$, the cylinder wake becomes unstable to three-dimensional perturbations with a spanwise wavelength of 3.96 diameters (d). A second instability on the two-dimensional base flow was found at $Re = 259$, with a spanwise wavelength of $0.822d$. These instabilities and their respective spanwise wavelengths agree closely with experimental observations of the mode A and mode B wake structures observed experimentally by Williamson (1988*b*). Three-dimensional

simulations by Thompson, Hourigan & Sheridan (1994, 1996) captured detailed images of the saturated three-dimensional streamwise vortical structures corresponding to these two different bifurcations.

Henderson (1997) performed three-dimensional simulations on the wake of the circular cylinder through the mode A and mode B transitions. The span of the simulations was varied up to 4 times the spanwise wavelength of the mode A instability. The interaction between the mode A and mode B instabilities was studied by monitoring the energy present in the various spanwise Fourier modes of the simulations. Wake visualizations were captured at $Re = 265$ showing the coexistence of both mode A and mode B wake structures. This spontaneous switching between one mode and the other may explain the presence of two distinct Strouhal frequencies in the wake in the Reynolds-number range $230 < Re < 260$ as observed by Williamson (1988*b*). An attempt was made to study the physical mechanism leading to the formation of streamwise vortical wake structures (Mittal & Balachandar 1995); however, the computational domain only spanned a single cylinder diameter, resulting in the artificial suppression of mode A structures. They did, however, observe the formation of well-defined vortical structures in the braid region of the vortex street, associated with mode B shedding. A detailed Floquet analysis was performed (Thompson, Leweke & Williamson 2001*b*) in an attempt to identify the physical mechanism of the mode A transition showing, although complex, it is consistent with an elliptic instability of the vortex cores. Evidence suggests that the transition is in fact a cooperative elliptic instability (Leweke & Williamson 1998), with the elliptic instability dominant in initiating the growth of the three-dimensional flow structures in the near wake. Advection then transports some perturbation into the braid regions as the wake convects downstream.

A geometric analogy exists between the two-dimensional circular cylinder placed close to a wall, and the circular cross-section bluff ring at small aspect ratios, where the ring cross-section lies in the vicinity of the axis. Essentially, both the axis of the ring and the boundary near the cylinder constrain and deform the resulting wake. A free surface with a Froude number ($Fr = 0$) dominated by gravity is essentially a boundary with zero tangential stresses. Hourigan, Reichl & Thompson (2002) modelled such a case with numerical simulations at a Reynolds number $Re = 180$. They showed that as the cylinder approached the free surface, the Strouhal number for the vortex shedding street increased by 10% from the reference cylinder with no boundaries in its vicinity. This maximum shedding frequency occurred where the gap between the cylinder and the wall was 0.7 times the diameter of the cylinder ($0.7d$). A further reduction in this gap saw a rapid drop in frequency, until for gap ratios less than $0.1d$ no vortex shedding was observed. The numerical bluff ring study by Sheard *et al.* (2001) presents Strouhal-number profiles showing a similar reduction in Strouhal number with decreasing aspect ratio (i.e. a decreasing gap between the axis and the circular ring cross-section) to the work of Hourigan *et al.* (2002). Despite this, no Strouhal-number rise with decreasing aspect ratio can be found for bluff rings, although a small rise in Strouhal number as the gap ratio approached $0.7d$ was observed for the cylinder near a free surface.

1.3. *Square cylinder wake*

When studying the three-dimensional stability of the square cylinder, Robichaux *et al.* (1999) found an intermediate wavelength mode ($2.8d$) that they designated mode S. This mode was periodic over two shedding cycles of the base flow (2T symmetry). This symmetry is in contrast to modes A and B, which are periodic over a single period of

Sphere transition type	Reynolds number
Boundary-layer separation	20
Regular asymmetric transition – regular bifurcation	210 to 212
Hopf transition – Hopf bifurcation	270 to 280

TABLE 1. Transition Reynolds numbers for the wake around a sphere (Johnson & Patel 1999; Tomboulides & Orszag 2000).

Circular cylinder transition type	Reynolds number
Boundary-layer separation	4 to 5
Hopf transition – Hopf bifurcation	47
Three-dimensional transition – Hopf bifurcation	188.5

TABLE 2. Transition Reynolds numbers for the wake around a circular cylinder (Noak & Eckelmann 1994*b*; Williamson 1988*a*; Barkley & Henderson 1996).

the base flow (1T symmetry). Their study also found analogous mode A and mode B instabilities in the wake; however, the spanwise wavelengths of both modes were about 40% larger than those for a circular cylinder. This is consistent with the diagonal length being the dimension controlling the scaling of the spanwise wavelengths of the instability modes for this particular geometry. The mode S topology and periodicity is identical to the mode C instability observed for the circular cylinder wake (Zhang *et al.* 1995) when a tripwire is placed close to the body. The wavelength of the mode C instability was predicted to be $2d$. The circular cylinder wake has not been found to exhibit this mode C type instability without artificial forcing.

A summary of the sphere and cylinder transitions is presented in tables 1 and 2, respectively.

1.4. *Wake of a toroidal body*

A bluff-body geometry that spans the extremes of wake behaviour shown by the sphere and circular cylinder as a single geometric parameter is varied, is the torus (or ring) with its axis placed parallel to the flow. This particular geometry has been studied previously by Leweke & Provansal (1995), with the main motivation to remove the end effects that experimentally hinder circular cylinder wake studies.

The parameters specifying the bluff ring geometry are defined as in Leweke & Provansal (1995), consistent with earlier work by the current authors. We define the aspect ratio as $Ar = D/d$, where D is the major diameter of the circular centreline of the ring cross-section, and d is the minor diameter of the cross-section of the ring. The geometry is represented schematically in figure 1. By varying the single geometric parameter Ar, a uniform axisymmetric body is described varying from a sphere at $Ar = 0$, to a straight cylinder in the limit $Ar \to \infty$. The hole in the centre of the ring first appears at the axis at $Ar = 1$.

The Reynolds number is based on the uniform free-stream velocity, U, the length dimension d, and the kinematic viscosity, ν, consistent with the previous definitions for both the sphere and cylinder.

The flow around a bluff ring has been afforded limited attention in the literature. Roshko (1953) showed experimentally that laminar vortex shedding from rings occurred at frequencies lower than for the circular cylinder by up to a few per cent. This behaviour was quantified experimentally by Leweke & Provansal (1995). They defined a Strouhal–Reynolds-curvature relationship for laminar shedding for a ring diameter

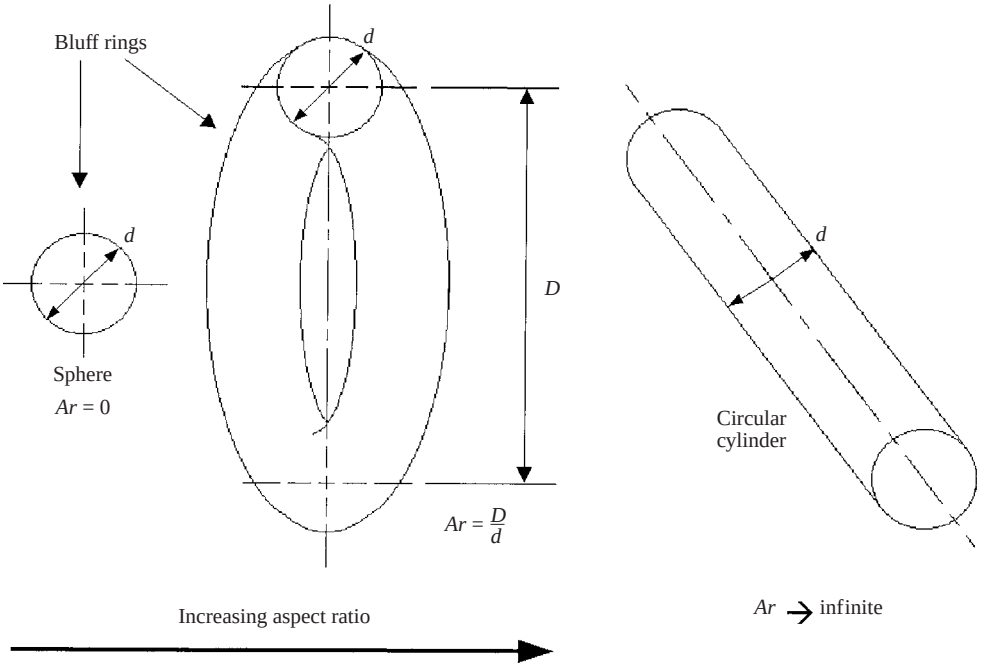

FIGURE 1. Schematic diagram of the bluff ring system.

at least 10 times greater than its cross-sectional diameter. Their study also investigated the transition regimes for $Re < 400$, modelling the straight circular cylinder wake without end effects as a torus. Roshko (1953) noted that at smaller aspect ratios, the ring wake exhibited a vastly different Strouhal–Reynolds number variation. The numerical investigation by Sheard *et al.* (2001) complemented these experimentally derived Strouhal profiles for the range of aspect ratios $5 \leqslant Ar \leqslant 40$.

The analogy between the wakes of spheres and disks and those of rings with aspect ratios $Ar < 5$ was investigated at Reynolds numbers $Re = 10^4$ by Bearman & Takamoto (1988). Their findings supported the observations of Roshko (1953) pertaining to the low-aspect-ratio ($Ar < 5$) behaviour. The Reynolds numbers they studied were far larger than in the present study; here, only the range $Re < 400$ is considered, consistent with the range over which transitions to unsteady asymmetric flow are expected.

Asymmetric wakes were observed by both Monson (1983) and Leweke & Provansal (1995), in the form of helical vortex rings analogous to the oblique shedding observed by Williamson (1989) for circular cylinders. Whereas the oblique wake of a circular cylinder can be observed at arbitrary angles to the cylinder axis depending on the experimental end conditions and cylinder length, the helical vortex rings were observed to shed as discrete modes consisting of single, double or triple helices. This is due to the imposed periodicity of the bluff ring geometry. The experiments of Monson (1983) involved observing a ring falling through a liquid, rendering Strouhal-number measurements difficult. However, the study by Leweke & Provansal (1995) involved passing fluid over a fixed ring, which allowed accurate measurements of the Strouhal number. The appearance of the three helical modes was studied for different aspect ratios, and it was found that the double and triple helices could only be observed for larger rings of aspect ratio approximately $Ar > 18$. The stability of the helical modes

was also studied. Higher-order helical modes were less stable, being observed only at higher Reynolds numbers than for parallel shedding. Furthermore, it was observed that a decrease in aspect ratio led to a corresponding increase in the relative critical Reynolds numbers for the respective helical modes.

The Strouhal–Reynolds number profiles of Leweke & Provansal (1995) over the asymmetric transition range for the bluff rings compare in an interesting way to the corresponding profiles reported by Williamson (1988*a*, 1996) for the circular cylinder. The former observed a discontinuity, marked by a drop in Strouhal frequency of about 5%, in the vicinity of the mode A transition for the cylinder, consistent with the corresponding drop in the cylinder profile. At the mode B transition, however, Strouhal-number profiles for the ring exhibit a difference in the behaviour. For the circular cylinder, there is evidence of two distinct frequencies in an overlap region before the wake becomes dominated by the mode B instability at $Re \approxeq 260$. In contrast, the wake of the bluff ring appears to undergo a continuous transition as the Reynolds number increases. At higher Reynolds numbers ($Re > 300$), there is a return to consistency between the cylinder and ring profiles for the range of aspect ratios studied.

At present, no understanding of the transition regimes that exist over the aspect ratio parameter space for the bluff ring is known. The axisymmetric computations and associated linear stability analysis of the present study enables both axisymmetric and primary asymmetric instabilities of the bluff ring wakes to be predicted, and a corresponding stability parameter space for all bluff rings to be mapped.

1.5. *Structure of paper*

The remainder of the paper consists of the following sections: numerical formulation, axisymmetric flow characteristics, axisymmetric wake stability, linear asymmetric wake stability, asymmetric flow visualization, and discussion and conclusions. The numerical formulation section outlines the numerical methods used for both the axisymmetric and asymmetric flow simulations, and the linear stability analysis of the axisymmetric flow to asymmetric perturbations. The following section on axisymmetric flow characteristics summarizes and expands on the Strouhal-number profiles of the system. Flow visualizations are provided and compared to the wakes of the reference wake flows of the sphere and cylinder. The section covering axisymmetric wake stability provides profiles of the transition from attached to separated flow, as well as the transition to unsteady flow for the axisymmetric wakes. Mathematical fits describing these transitions are provided, as well as for the Strouhal number as a function of both the Reynolds number and aspect ratio. Results of linear stability analysis are then presented. As well as highlighting the dominant shedding modes and visualizing the acquired perturbation fields of both steady and unsteady wake flows, the change in the dominant azimuthal instability mode with aspect ratio will also be considered. The final results section presents the predicted behaviour of the critical Reynolds number for the transition to unsteady flow from the steady asymmetric wakes of rings with $Ar < 4$.

2. Numerical formulation

2.1. *The spectral-element method*

A spectral-element method was used for the numerical simulations in this investigation. This method is described in detail in Patera (1984), Karniadakis (1990), and Thompson *et al.* (1994, 1996), so only a brief outline is provided here. The

spectral-element method is based on the Galerkin finite-element method, incorporating high-order Lagrangian polynomial shape functions within each element. The node points of the Lagrangian polynomials correspond to the Gauss–Legendre–Lobatto quadrature points, allowing accurate and efficient integration over each element. For non-axisymmetric calculations, axisymmetric grids were expanded in the azimuthal direction using a Fourier expansion, allowing asymmetric evolution of the flow fields.

The axisymmetric and asymmetric formulation of the code has been applied successfully to both the sphere (Thompson *et al.* 2001*a*), and the circular cylinder (Thompson *et al.* 1994, 1996), so further validation is not presented here.

The axisymmetric simulations are sufficient to determine both the critical Reynolds numbers for transitions to separated wake flow, and the subsequent axisymmetric transition to unsteady flow. To determine the wake stability of the axisymmetric base flow to asymmetric perturbations, application of Floquet stability analysis is undertaken.

2.2. *Linear Floquet stability analysis*

Floquet stability analysis can be used to determine the stability of a periodic axisymmetric base flow to asymmetric perturbations. Barkley & Henderson (1996) applied this technique successfully to study the asymmetric transitions of the straight circular cylinder. Natarajan & Acrivos (1993) performed a similar study for the stability of the sphere wake. Both the sphere wake stability results, as well as the straight circular cylinder results are replicated in this paper to validate the current formulation and implementation of the stability analysis technique. The present numerical technique has been successfully applied to the wake of a circular cylinder (Thompson *et al.* 2001*b*). The asymmetric Floquet modes are determined from the linearized Navier–Stokes equations assuming sinusoidal variation in the azimuthal direction with mode number, m. This corresponds to a spanwise wavelength of $\lambda = 2\pi/m$ for the bluff ring geometry. In the cylindrical polar coordinate formulation of this technique, the wavelength is expressed in radians. Only integer mode numbers are considered, as the azimuthal wavelength must be a whole factor of 2π radians because of periodicity imposed by the geometry. The implementation of the method in this case is similar to the implementation of Barkley & Henderson (1996). Effectively, the perturbation field satisfying the linearized Navier–Stokes equations is evolved at each time step in parallel to the base flow. The L_2 norm of the perturbation field is normalized to unity at the beginning of each period, and the global growth or decay of the perturbation field is measured at the end of each period. This gives the amplitude growth factor which converges after many periods to the dominant Floquet multiplier (μ) of the system for a given Reynolds number and spanwise wavelength λ (or equivalent m). Floquet multipliers $\mu > 1$ indicate an exponentially growing perturbation and hence an unstable base flow. Conversely, if the multipliers for all possible wavelengths are less than unity, the base flow is stable. A Floquet multiplier of $\mu = 1$ represents neutral stability, where an imposed low-amplitude perturbation neither grows nor decays. The aim is to determine the critical Reynolds numbers and wavelengths at which neutral stability is reached.

2.3. *Validation of spectral-element method and stability analysis technique*

The implementation of the spectral-element method used here is the same as that employed by Thompson *et al.* (1994, 1996), and Sheard *et al.* (2001, 2002), hence only validation of the meshes used is necessary.

A thorough grid-resolution study determined an acceptable compromise between computational efficiency and allowable accuracy in this investigation. After considerable testing, meshes consisting of approximately 400 elements were found to resolve the flow field within an accuracy of better than 1%. Blockage and outflow boundary effects were minimized by employing domain sizes for the inlet, outer transverse domain and outlet of 15, 30 and 25 units, respectively. These domain sizes maintained an accuracy for global wake parameters of better than 1%, 0.1% and 0.1%, respectively. Elements with 64 nodes (8×8) were used predominantly; however, in order to retain an accuracy of better than 1% for $Re > 300$, elements with 81 (9×9) nodes were used.

For small aspect ratios, and especially those in the vicinity of $Ar = 1$, where the ring exhibits singular points on the axis upstream and downstream, careful attention was paid to the meshing of these cases to limit the skewness of mesh elements, and to include sufficient spatial resolution in the vicinity of the ring to model the flow, as discussed in the next paragraph. To ensure the consistency between the axisymmetric and asymmetric formulations of the numerical scheme, a computation was performed using both methods for an $Ar = 1.2$ ring at $Re = 300$, with asymmetric flow suppressed. Both methods provided global quantities such as the drag coefficient to within 0.5%, and a measure highly sensitive to numerical accuracy, the velocity components at a point in the wake were within 0.9%.

An approximate boundary-layer thickness (δ) is analytically calculated at several points around the bluff ring cross-section for flow at a Reynolds number $Re = 300$. At distances from the front to the rear of a quarter, a half, and the full distance, the thickness was estimated as $0.18d$, $0.26d$ and $0.36d$. The macro-element closest to the ring cross-section for all meshes employed in this study is $0.0872d$ thick, and the second element extends to $0.2383d$. Thus, even with a polynomial order of only $N^2 = 64$, between 11 and 19 nodes resolve the boundary layer around the ring cross-section.

As mentioned above, the Floquet stability analysis technique was validated by comparing results obtained for both the straight circular cylinder wake and the sphere wake, with accepted values from experiment and numerical work.

A numerical stability analysis of the sphere wake has been performed by Natarajan & Acrivos (1993). They determined that the sphere wake becomes asymmetric at a Reynolds number $Re = 210$, undergoing a regular bifurcation and adopting a non-axisymmetric wake with a mode number $m = 1$.

For the current validation exercise, Floquet analysis conducted on the steady axisymmetric flow around a sphere was carried out over several Reynolds numbers to determine the neutral stability for the $m = 1$ mode of the wake. Quadratic interpolation over Reynolds number indicated that this transition occurred at $Re = 211.5$. Note that this value is in good agreement with the numerical stability analysis of Natarajan & Acrivos (1993), the numerical simulations of Tomboulides & Orszag (2000), and the experimental studies by Johnson & Patel (1999).

A similar study was performed for the flow past a straight circular cylinder. Barkley & Henderson (1996) predicted the critical Reynolds number for mode A shedding to be $Re = 188.5 \pm 1.0$ at a wavelength of $\lambda = 3.96 \pm 0.02$. For the present study, Floquet multipliers were obtained at 7 discrete wavelengths over the range $3.9 \leqslant \lambda \leqslant 4.02$ and at 3 distinct Reynolds numbers in the range $185 \leqslant Re \leqslant 190$. The critical transition was estimated using cubic interpolation over the spanwise wavelength and quadratic interpolation over the Reynolds number. The critical Reynolds number for the onset of mode A shedding was found to be $Re = 188.3$ with a spanwise wavelength of

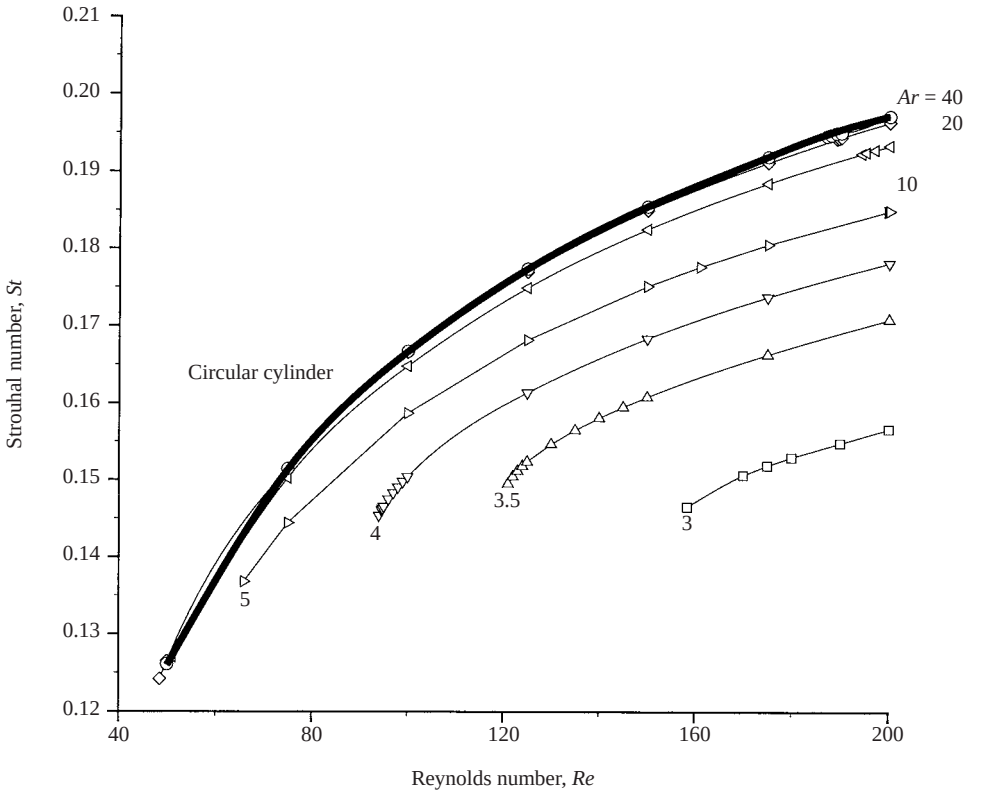

FIGURE 2. Computed Strouhal–Reynolds-number profiles for the axisymmetric flow around bluff rings. The solid black line highlights the circular cylinder Strouhal number profile for reference. Although axisymmetric profiles of the $Ar = 3$ and $Ar = 3.5$ rings are presented, it will be shown later that the wakes of these rings would in fact be asymmetric for these Reynolds numbers.

$\lambda = 3.96$. These values are within the error bounds of the previous studies, validating both the resolution and domain size of the meshes used, and also the stability analysis code. Furthermore, they indicate that both dominant modes and the corresponding critical Reynolds numbers will be found with an accuracy of better than 1%.

3. Results: axisymmetric flow characteristics

Strouhal–Reynolds-number profiles have been computed for the periodic flow around bluff rings from axisymmetric simulations. These numerical predictions are compared with the experimental results of Leweke & Provansal (1995). Strouhal–Reynolds-number profiles are computed for a circular cylinder, and bluff ring models of aspect ratios $Ar = 3$, 5, 10, 20 and 40. The significant variation between the Strouhal-number curves for the $Ar = 3$ and $Ar = 5$ rings prompted further simulations at intermediate aspect ratios $Ar = 3.5$ and $Ar = 4$. The profiles for these rings are also included in figure 2, which shows the Strouhal profiles obtained for the current set of bluff ring aspect ratios.

Figure 2 shows a distinct trend towards the Strouhal number profile for the straight circular cylinder with increasing aspect ratio for the bluff ring Strouhal number profiles. An increase in the critical Reynolds number for the onset of periodic flow is

also observed as aspect ratio decreases. Rings with $Ar > 10$ exhibit periodic shedding within 5% of the corresponding circular cylinder transition, whereas rings with smaller aspect ratios ($Ar < 10$) undergo the transition at successively higher Reynolds numbers as the aspect ratio decreases. Furthermore, the Strouhal number at the onset of vortex shedding shows an increasing trend as the aspect ratio is decreased towards $Ar \to 3.5$. The initial Strouhal number for the $Ar = 3$ ring is slightly lower than the $Ar = 3.5$ ring.

The following sections discuss the determination of the critical Reynolds numbers for the transition to separated flow, and the transition to unsteady flow. In addition, some of the features of the flow fields observed in the investigation are elucidated, and a universal empirical fit for the Strouhal number as a function of both Reynolds number and aspect ratio is proposed.

3.1. *Transition to separated flow*

To determine the initial wake transition from attached to separated wakes, flow separation was determined by monitoring the stagnation points around the cross-section of the ring. A single upstream stagnation together with a single downstream stagnation indicates fully attached boundary layers around the inner and outer ring surface. More than two stagnation points on the torus cross-section indicate that flow separation has occurred, and reversed flow is present in the wake. An alternative to this approach for quantifying this transition is to measure the recirculation bubble length at Reynolds numbers beyond the transition, and extrapolating the length to zero against Reynolds number (see Tomboulides & Orszag 2000). However, for the torus, the position and orientation of the recirculation zones varied with aspect ratio and Reynolds number, hence the bubble lengths are more difficult to measure consistently. Results for the straight cylinder and the sphere were obtained along with those of the bluff rings to verify consistency with values in the literature. For both the sphere and the circular cylinder, the present results agreed with previous findings to the limit of experimental and numerical error ($Re \pm 0.5$). A graph of the transition Reynolds number, Re_{T1}, for flow separation against aspect ratio is provided in figure 3.

Two distinct types of separation can be inferred from figure 3. The first type occurs to the left of the asymptote (dotted line) for $Ar \leqslant 1$, and the other for aspect ratios $Ar > 1$. The discontinuous behaviour of the separation transition is understandable when we consider the discontinuous topological change at $Ar = 1$.

Recall that aspect ratios $Ar > 1$ represent a ring with a hole present at the axis, whereas those geometries with $Ar \leqslant 1$ have no hole present. Hence in the $Ar \leqslant 1$ region, the transition leads to a recirculation bubble in the wake behind the ring on the axis. An increase in aspect ratio from the sphere at $Ar = 0$ in turn increases the maximum angle at which fluid has to remain attached around the leeward side of the ring geometry to greater than 90° to the direction of the flow. As $Ar \to 1$, the fluid would have to deflect so far around the rear of the ring and towards the axis that to remain attached, the fluid would need to travel in the upstream direction parallel to the axis. This explains the decrease of the transition from the sphere transition at $Re = 21$ towards zero over the range $0 \leqslant Ar \leqslant 1$. At aspect ratios $Ar > 1$, fluid passes through the hole, changing the character of the separation bubble.

Figure 4 shows streamlines at an aspect ratio $Ar < 1$, after the transition to separated flow. Note the recirculation bubble behind the ring cross-section centred on the axis.

The flow separation profile for $Ar > 1$ involves the development of a local flow separation bubble behind the circular ring cross-section. Hence, instead of the axial

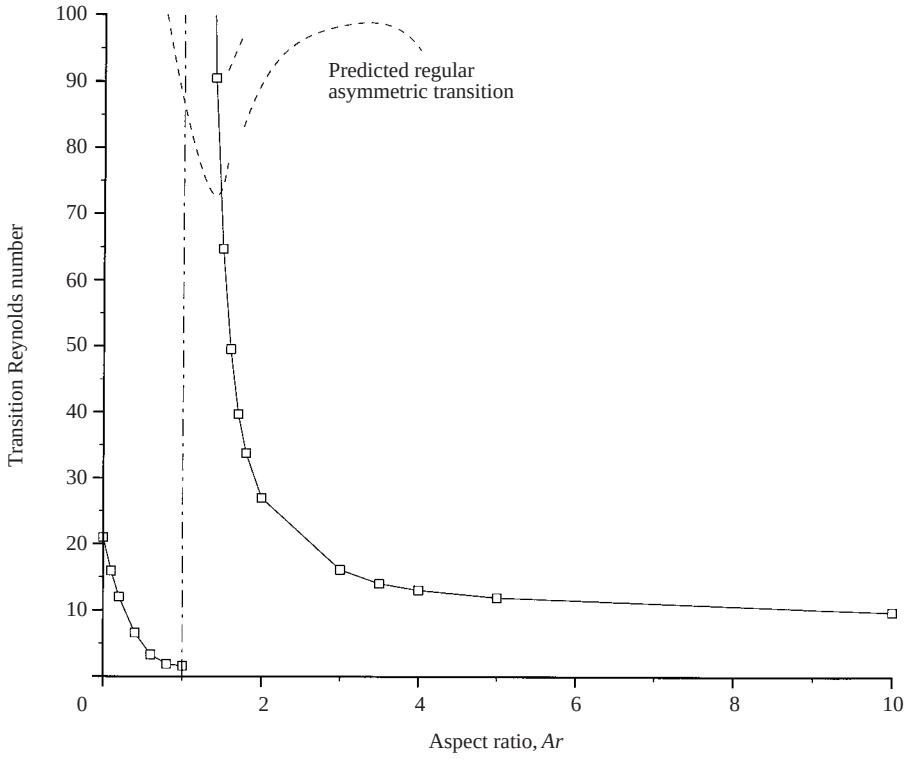

FIGURE 3. Reynolds numbers for the flow separation transition (Re_{T1}) versus aspect ratio for bluff rings. The dashed line indicates the emergence of the hole in the centre of the torus at $Ar = 1$. The predicted asymmetric transition profile is marked by a dotted line, marking the limit of validity for the axisymmetric computations (see figure 15).

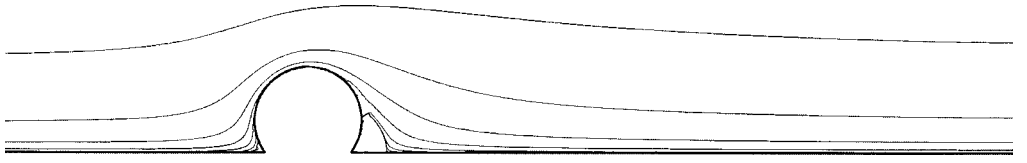

FIGURE 4. Flow streamlines around a ring of aspect ratio $Ar = 0.6$ at $Re = 10$, following the separation transition, illustrating the recirculating region behind the ring on the axis. Unevenly spaced streamline contour levels are used to elucidate relevant flow structures.

recirculation bubble found for $Ar \leqslant 1$, a distinct recirculating ring of fluid is formed behind the downstream surface of the torus. For aspect ratios in the range $1 < Ar \leqslant 3$, the transition occurred at much higher Reynolds numbers than for the sphere and cylinder transitions. This will be explored in the following section. For larger aspect ratios ($Ar > 3$), the transition is found at Reynolds numbers similar to that of the corresponding circular cylinder transition. Figures 4 and 5 highlight the difference between the transition for rings of $Ar \leqslant 1$ and $Ar > 1$. In figure 5, the flow past a ring with aspect ratio $Ar = 3$ is shown at $Re = 100$, following the transition. The recirculation zone is clearly visible downstream of the circular ring cross-section, and the flow field is steady.

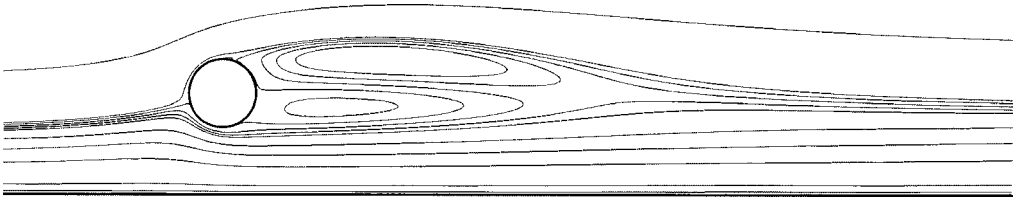

FIGURE 5. Flow streamlines around a ring with aspect ratio $Ar = 3$ at $Re = 100$, following the separation transition, illustrating the recirculating region behind the ring cross-section. Arbitrary contour levels are used to highlight the flow structures.

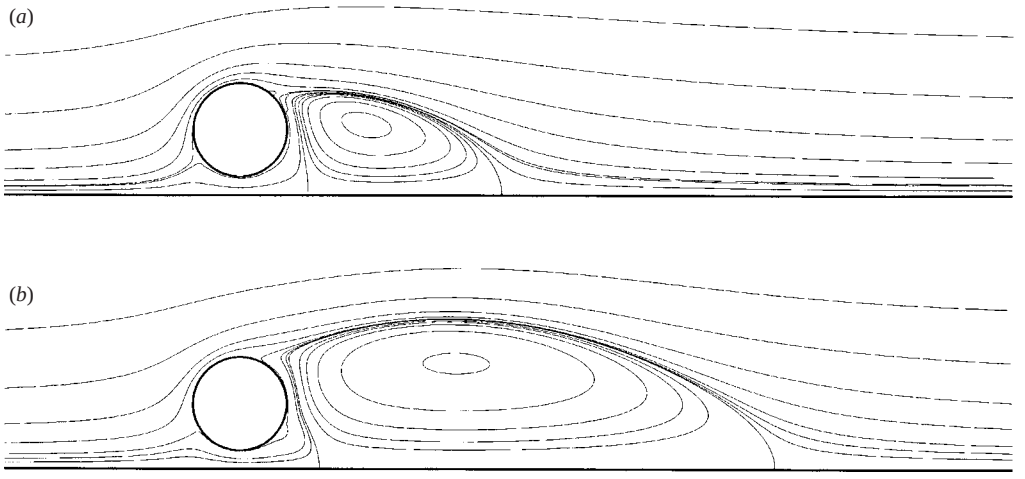

FIGURE 6. Flow streamlines around a ring with aspect ratio $Ar = 1.4$. Part (a) shows a computation at $Re = 25$, showing the axial recirculation bubble located downstream of the ring. Part (b) shows a computation at $Re = 100$, with a larger axial recirculation bubble located downstream of the ring. Note also the divergence of streamlines in the lower right-hand surface of the ring cross-section, corresponding to the impending flow separation transition. Again, the contour levels of the streamline plots are arbitrary.

3.2. *Detached recirculation bubble on axis*

Observation of the velocity fields at aspect ratios $1 < Ar \leqslant 2$ show an interesting physical phenomenon mentioned in the preceding section. Rings with no hole ($Ar \leqslant 1$) exhibit a single axial recirculation region downstream, similar to the case of the sphere. However, at an aspect ratio larger than $Ar = 1$, the presence of the hole in the ring on the axis results in a detached recirculation bubble on the axis downstream of the body, as shown in figure 6(a). This bubble increases in size with Reynolds number, but is not observed for larger aspect ratios (approximately $Ar > 2$). The bubble exists owing to the stagnation of fluid on the axis downstream of the ring resulting from an adverse pressure gradient induced by the divergence of fluid radially outward around the leeward surface of the bluff ring. This effect is negated at higher aspect ratios, as the geometric radial divergence is not as significant near to the axis. Note the absence of any such axial recirculation in figure 5. Figure 6(a) shows such a recirculation bubble downstream of the ring cross-section for a ring with $Ar = 1.4$ at $Re = 25$. The upstream streamlines indicate that all but a column of fluid approximately $0.1d$ in diameter is deflected around the outside of the ring.

The ring cross-section in figure 6(*a*) shows an upstream stagnation in the lower left-hand quadrant of the cross-section of the ring, and a corresponding downstream stagnation is located on the upper right surface of the cross-section. Observe that no evidence of boundary-layer separation can be seen on the ring cross-section surfaces normal to the upstream and downstream stagnation points, that correspond to a leading and trailing stagnation ring in axisymmetric space. At the downstream stagnation, an artefact of the streamline integration is observed as a minute closed streamline.

A higher-Reynolds-number streamline plot for the same aspect ratio is shown in figure 6(*b*) where the first stages of boundary-layer separation at the inner downstream (bottom right) region of the ring cross-section are shown. This is the point where the streamlines deflect from the body before returning to a more coincident path around the trailing surface.

The increasing transition Reynolds number for flow separation as the aspect ratio decreases towards $Ar = 1$ may be explained by considering the streamline plots in figure 6. The restriction imposed by the small aspect ratio on the wake flow is clear when we consider both the small proportion of fluid passing through the middle of the ring in figure 6, and the high angle between the line through upstream and downstream stagnations and the horizontal. Observe that the fluid passing through the axial hole of the ring actually diverges as it approaches the body. This causes a local deceleration of the flow, which in turn lowers the local Reynolds number. Increasing the global Reynolds number of the system (compare figure 6*b* to figure 6*a*) allows a greater proportion of fluid to pass through the centre of the ring, hence forming a stagnation and separation on the inner-downstream surface of the ring owing to the adverse body curvature in the vicinity. Thus, owing to viscous effects, smaller aspect ratios require a higher Reynolds number for sufficient fluid to pass through the centre of the ring to form a stagnation point and flow separation.

3.3. *The onset of unsteadiness in the bluff ring wakes*

The critical Reynolds numbers for the transition from steady to periodic flow was found by measuring the decay rate of unsteady velocity transients in the wake at a series of Reynolds numbers just prior to the onset of unsteady flow. Extrapolation of these decay rates to zero provides the Reynolds number corresponding to the neutral stability limit of unsteady transients in the steady axisymmetric wake. The Reynolds number at which this neutral stability is reached is the Hopf transition Reynolds number for unsteady flow, Re_{T2}. An example of the linear fit shown in figure 7, for the $Ar = 5$ ring.

A similar analysis was performed for a range of aspect ratios that exhibited periodic flow, specifically $Ar = 2$, 3, 3.5, 4, 5, 10, 20, 40, and the straight circular cylinder. Later in this paper results of a linear stability analysis are presented that predict that a regular asymmetric wake transition will precede the axisymmetric Hopf bifurcation of the steady wake for aspect ratios $Ar \lesssim 4$. We present the results of the axisymmetric study here in its entirety for completeness, however, regions of the axisymmetric parameter space that are predicted to be non-physical because of a prior asymmetric transition are represented by dotted lines.

Figure 8 provides the variation of Reynolds number, Re_{T2}, for the transition from steady to periodic flow obtained from the axisymmetric studies. Unsteady flow was not observed for aspect ratios $Ar < 1$; a result that was expected based on the observed behaviour of sphere and disk wakes that become unsteady only after a prior transition to an asymmetric wake. Obtaining the transition Reynolds numbers for $Ar < 2$ requires either fully asymmetric simulations, or the application of stability

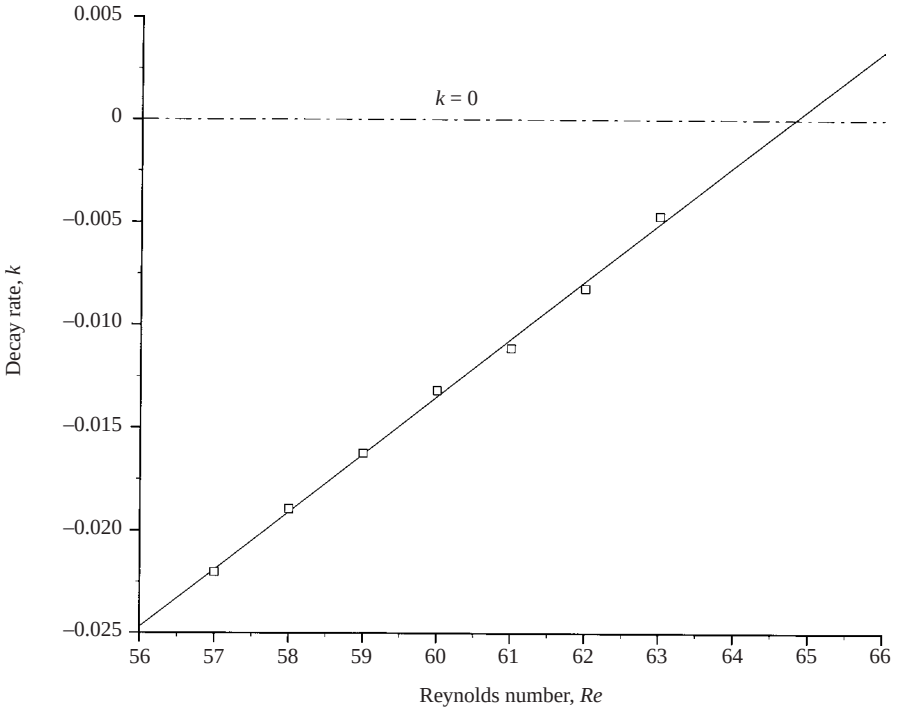

FIGURE 7. Unsteady transient decay rates for the $Ar = 5$ ring. Computed decay rates are shown as squares, and the solid line represents a linear fit to the data. The dashed line represents the neutral stability limit where the decay rate $k = 0$.

analysis, and will therefore be completed in later sections. Note that at the large aspect ratio limit, the unsteady transition asymptotes to that of the straight cylinder. This result is expected based on the studies of Leweke & Provansal (1995).

The dramatic increase in Re_{T2} as the aspect ratio decreases towards $Ar = 1$ is observed because the axisymmetric Hopf transition is an instability of the recirculating bubble behind the cross-section of the ring. Recall that the recirculating ring of fluid is formed following the separation transition Re_{T1}, which also increases rapidly as the aspect ratio approaches $Ar = 1$. These high transition Reynolds numbers allow asymmetry to develop in the wake of the bluff rings with small aspect ratios ($Ar < 4$ in fact) prior to the Hopf transition to unsteady flow. The sharp rise in Re_{T2} for the transition as the aspect ratio decreases towards $Ar = 1$ means that as the distance between the axis and the ring cross-section is decreased, a higher Reynolds number is required to sustain an unsteady wake. The work by Hourigan, Reichl & Thompson (2002) has been mentioned previously for the circular cylinder near a free surface. They saw a cessation of vortex shedding at $Re = 180$ for gap ratios less than $0.1d$. A ring with aspect ratio $Ar = 1.2$ has a similar gap ratio between the axis and ring cross-section; however, no vortex shedding is observed for aspect ratios $Ar < 2.7$ at $Re = 180$. It is probable that the higher solidity of the ring about the axis provides a greater constraint on the flow than the analogous circular cylinder near to a slip-wall. Therefore, greater Reynolds numbers are required to induce vortex shedding, although the mechanism inhibiting the unsteady wake is the same. A universal relationship for the Strouhal number as a function of both the aspect ratio, and the Reynolds number, is now developed.

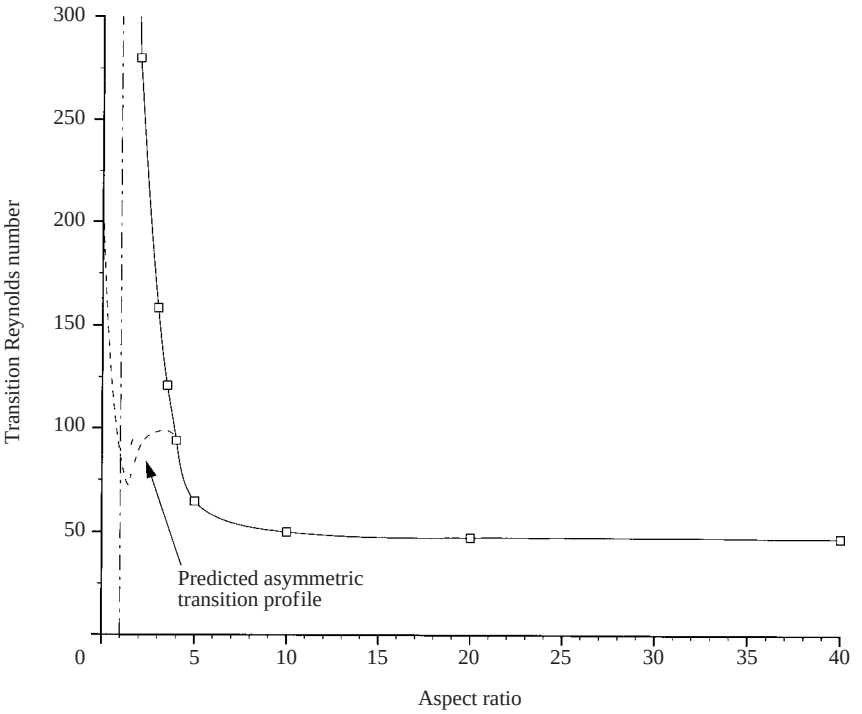

FIGURE 8. Reynolds numbers for the Hopf transition versus aspect ratio for bluff rings obtained from axisymmetric simulations. The dashed line indicates $Ar = 1$, where the hole first appears in the ring at the axis, and the dotted line marks the predicted asymmetric transition that defines the limit of validity of the presented axisymmetric Hopf transition results.

3.4. *Defining a Strouhal–Reynolds-number/aspect ratio relationship*

Leweke & Provansal (1995) proposed a relationship linking the Strouhal number to the Reynolds number and ring curvature (K) of a particular bluff ring. That extended the earlier work of Williamson (1988*a*) for the straight circular cylinder to non-zero curvatures. Williamson (1988*a*) noticed that the product of the Strouhal and Reynolds number in the axisymmetric regime is approximated closely by a quadratic function:

$$Re\,St = A\,Re^2 + B\,Re + C. \tag{3.1}$$

Ring curvature is related to aspect ratio by the relationship $K = 2/Ar$. The Strouhal-number relationship suggested by Leweke & Provansal (1995) extended Williamson's relationship to cover cylinders with non-zero curvature, as follows:

$$S(Re, K, \theta) = S_0(Re, K = 0) - a[Re - Re_c(K = 0)]K\cos(\theta). \tag{3.2}$$

Here, θ specifies the angle of the vortex street being shed with respect to the body axis. As these simulations are axisymmetric, no oblique shedding modes can be predicted, so the angle becomes $\theta = 0$. From experiment, they obtained the factor $a = 0.0002134$. Correcting the results in figure 2 for zero curvature $K = 0$, all the points should lie along the straight circular cylinder Strouhal-number profile included in the chart, if the relationship is in agreement with the current results. Figure 9 shows the result of this correction.

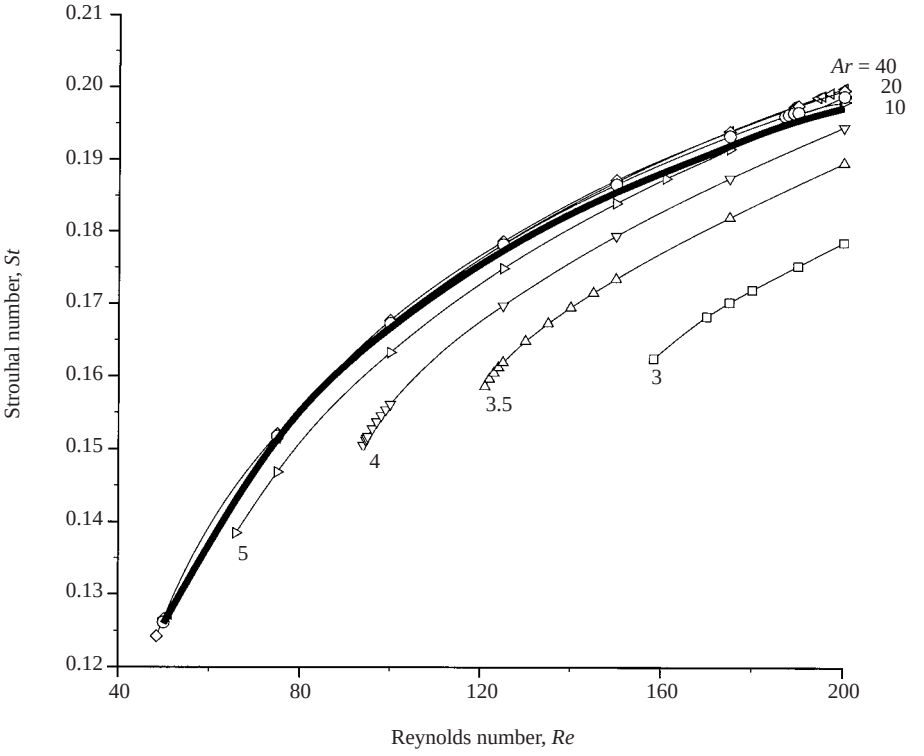

FIGURE 9. Strouhal–Reynolds-number profiles of the current data extrapolated to zero curvature using the curvature correction formula developed by Leweke & Provansal (1995). Recall that the flow for the $Ar = 3$ and $Ar = 3.5$ rings would in fact be asymmetric.

It is observed that the curves for smaller aspect ratios fail to collapse onto a single profile. This is due to a linear approximation in the relationship that loses validity for larger curvatures. As mentioned earlier, the study of Leweke & Provansal (1995) considered aspect ratios $Ar > 10$, as they were attempting to approximate wakes from a straight circular cylinder. The rescaled Strouhal-number profiles for rings of aspect ratio $Ar < 10$ in the present study fall successively under the ideal straight cylinder profile owing to an apparent nonlinear curvature dependence.

The previous relationship is of the form $S = S_0 - g(Re)K$. Here, the function $g(Re)$ is a linear function of Re independent of K, and it represents $|\Delta S_0/\Delta K|$. ΔS_0 is the difference between the bluff ring Strouhal number, and the corresponding straight cylinder Strouhal number at the same Reynolds number.

We propose a new functional dependence, based on the observation that the Strouhal–Reynolds-number profiles all exhibit a similar profile when translated to the same starting point, and scaled by a factor that varies with aspect ratio.

$$A\{S(Re, Ar) - S_c\} = \{S_0(Re - Re_c + Re_{0c}) - S_{0c}\}. \tag{3.3}$$

In this relationship, $S(Re, Ar)$ is the Strouhal number for the given Re and Ar, S_c is the critical Strouhal frequency for a given Ar, $S_0(Re)$ is the straight circular cylinder Strouhal number for a given Re, Re_c is the critical Reynolds number for a ring of given Ar, Re_{0c} is the critical Reynolds number of the straight circular cylinder, S_{0c} is

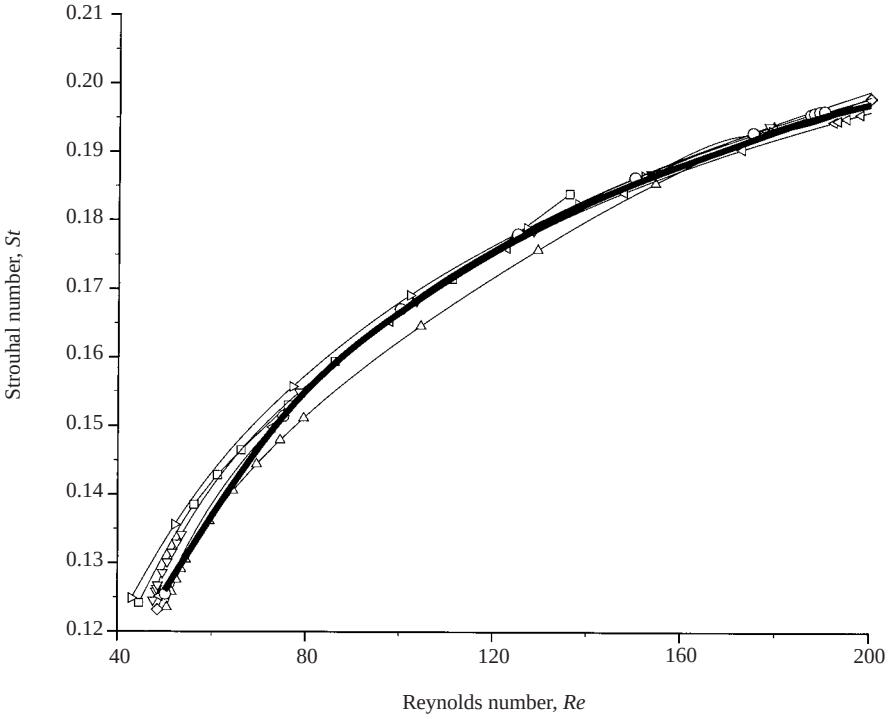

FIGURE 10. Bluff ring Strouhal–Reynolds-number profiles corrected to zero curvature using the proposed relationship. Symbols are as in figures 2 and 9.

the Strouhal frequency at the critical Reynolds number for the straight cylinder and A is the factor by which the Strouhal frequencies differ.

Introducing the ring curvature $K = 2/Ar$, the following relationships describe the above variables. These relationship forms were chosen to minimize error in determining the coefficients to less than 1%, as any discrepancy in these coefficients is amplified in the final result.

$$S_c = -1.1479K^5 + 0.59433K^4 + 0.34015K^3 - 0.12845K^2 + 0.0188K + 0.124,$$

$$S_0 = 4.524 \times 10^{-5} Re + 0.21335 - 4.9434/Re,$$

$$Re_c = 414.41K^3 - 16.516K^2 - 2.4113K + 46.511,$$

$$Re_{0c} = 46.511,$$

$$S_{0c} = 0.124,$$

$$A = 14.032K^3 - 4.8429K^2 + 0.72144K + 1.0.$$

To view the effectiveness of the proposed formula in predicting the Strouhal profiles, the bluff ring Strouhal numbers from figure 2 have been corrected to curvature $K = 0$. As can be seen in figure 10, they collapse close to one curve, belonging to the straight circular cylinder Strouhal profile. The maximum deviation of any one point from its predicted value is approximately 5%, but generally the deviation is much less than 2%. The fit provided by Leweke & Provansal (1995) is accurate to within 1% for rings with aspect ratios $Ar \geqslant 10$; however, for aspect ratios in the range $3 \leqslant Ar < 10$ the discrepancy can be as high as 15%. Over this aspect ratio range, the relationship derived by Leweke & Provansal (1995) typically predicts Strouhal frequencies with

a discrepancy an order of magnitude greater than the current expression. Note, however, that the linear stability analysis comprising the next section predicts that the wakes of rings with aspect ratios $Ar < 4$ undergo an asymmetric transition prior to the Hopf transition. The present formula still exceeds the accuracy of the Leweke & Provansal (1995) relationship, that exhibits errors of approximately 10% for the Strouhal number profile for an aspect ratio $Ar = 4$.

4. Results: linear asymmetric wake stability

4.1. *Determining asymmetric stability using Floquet analysis*

A detailed study of the stability of the bluff ring system to asymmetric perturbations using the Floquet analysis technique was performed.

Following the validation of the stability analysis code against the sphere and cylinder geometries discussed previously, the dominant shedding modes for the larger aspect ratio rings were determined, and also the critical transition Reynolds numbers for asymmetric flow of both the periodic and steady base flows observed for larger and smaller aspect ratio rings, respectively.

The spanwise wavelengths and critical Reynolds numbers of the mode A and mode B transitions for the circular cylinder (Barkley & Henderson 1996) were used as a guide for the present stability analysis. Floquet multipliers were calculated at Reynolds numbers in the vicinity of the critical transitions of the dominant modes. Cubic and quadratic interpolations were used to more accurately estimate the critical Reynolds numbers and spanwise wavelengths of the transitions. Note that critical Reynolds numbers found for secondary transitions should be treated with caution as once the flow has undergone a lower-Reynolds-number asymmetric transition, the axisymmetric base flow used for the analysis is no longer applicable. Barkley & Henderson (1996) offer a description of the limitations of linear stability theory.

The first-occurring asymmetric vortex-shedding mode in the cylinder wake with increasing Reynolds number predicted by the stability analysis of Barkley & Henderson (1996) was mode A. At a higher Reynolds number, another mode was predicted, mode B. The topological predictions of the mode B transition from the stability analysis compared favourably with experimental flow visualizations of the saturated mode (Williamson 1988*b*, 1996) in terms of both the spanwise wavelength of the asymmetric structures, and their spatio-temporal symmetry. Despite the accurate predictions relating to the structure of this second instability, experimental observations (Williamson 1988*b*) showed evidence of mode B structures in the wake at Reynolds numbers as low as $Re = 230$, 11% below the predicted transition Reynolds number from the stability analysis (presumably due to the change in the base flow).

A discrepancy between the prediction of the secondary asymmetric transition for the sphere and numerical simulations of the asymmetric wake can also be shown. Stability analysis performed by Natarajan & Acrivos (1993) highlights a second mode following the initial steady asymmetric transition in the wake of the sphere. This transition is from a steady asymmetric flow to an unsteady asymmetric flow, and was predicted to occur at $Re_{S3} = 277.5$. Numerical simulations of the sphere wake in the present study find unsteady flow for Reynolds numbers $Re_{S3} > 272$. The topology of the transition is in agreement with the stability analysis; however, the critical Reynolds number for the transition is 2% lower in simulations of the real wake than the predicted value from the stability analysis. It is inferred that the topology of secondary modes in the wake of the bluff ring will be predicted accurately by the stability analysis; however, only qualitative estimates of the critical Reynolds numbers

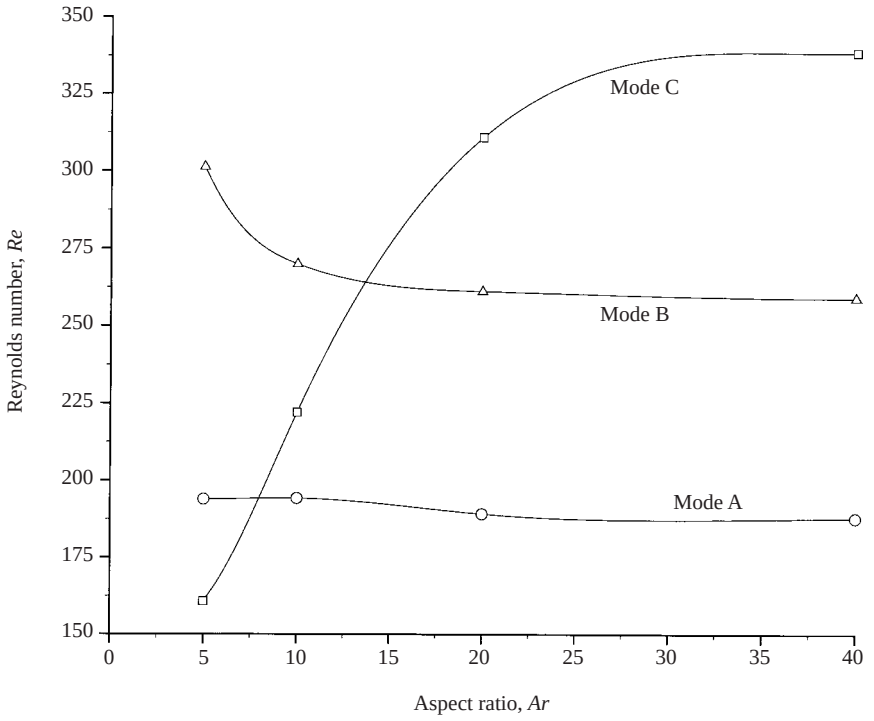

FIGURE 11. Critical Reynolds numbers for the transitions to the asymmetric vortex-shedding modes for large-aspect-ratio bluff rings. ○, mode A transition; △, mode B; □, mode C.

relating to secondary transitions can be made, generally accurate to within 15% of the actual values as determined by direct simulations.

Modes of asymmetric shedding in the unsteady flow fields associated with rings of aspect ratio $Ar \geqslant 5$ are presented in the next section. Later, smaller aspect ratios will be considered, where the dominant Floquet modes occurred for a steady base flow.

4.2. *Asymmetric shedding modes for* $Ar \geqslant 5$

Results for the stability of the periodic wakes of larger bluff rings will be presented first. Profiles of the critical transition Reynolds numbers for the asymmetric shedding modes of bluff rings as a function of aspect ratio are shown in figure 11. Figure 11 illustrates that asymmetric instabilities in these wakes occur close to the critical Reynolds numbers for both mode A and mode B instabilities for the straight cylinder. Note the presence of the third mode, referred to as mode C in this investigation. At aspect ratios $Ar \geqslant 20$, mode C becomes unstable at a higher Reynolds number than either mode A or mode B. The critical Reynolds number for the mode C transition decreases with decreasing aspect ratio, such that mode C becomes the first appearing mode for rings with $Ar = 5$.

For rings with an aspect ratio large enough to observe axisymmetric periodic vortex shedding ($Ar \geqslant 4$), the spanwise wavelengths at which the mode A and mode B transitions are most unstable corresponds closely with the respective wavelengths for the shedding modes of the circular cylinder wake. Figure 12, showing the Floquet multiplier as a function of spanwise wavelength for each mode at Reynolds numbers close to the transitions for the $Ar = 10$ ring, illustrates the similarity of the mode wavelengths of the bluff ring and circular cylinder wakes. The narrowband mode C

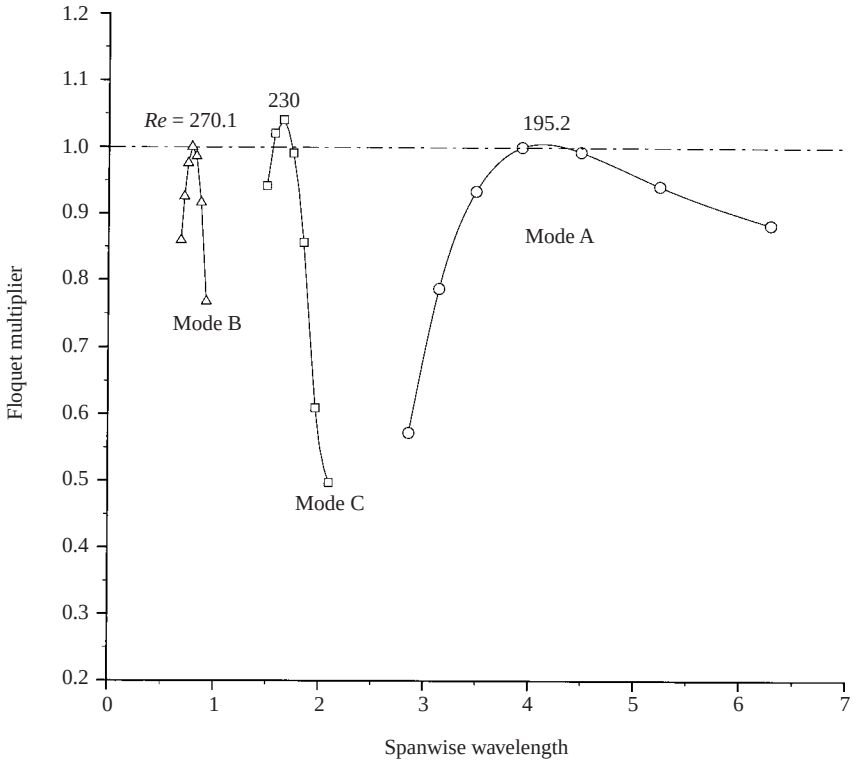

FIGURE 12. Floquet multiplier profiles for the $Ar = 10$ ring. Note the Reynolds number for each mode, and the spanwise wavelength at which they are least stable.

instability, located between the familiar mode A and mode B instabilities displayed in figure 12, has not been reported previously for unrestricted flow around a straight circular cylinder. Zhang *et al.* (1995) did, however, observe an asymmetric mode of a similar spanwise wavelength in the wake of a cylinder with a tripwire in the vicinity of the cylinder body. Robichaux *et al.* (1999) found a mode of a similar wavelength for the flow around a square cross-section cylinder which they denoted mode S. As discussed earlier, the mode C instability becomes more prominent as the aspect ratio is decreased, with the critical Reynolds number for the transition decreasing, and the bandwidth of the mode increasing, with decreasing aspect ratio.

Mode C has a spanwise wavelength between those of mode A and mode B, approximately $1.7d$. The mode C wavelength quoted by Zhang *et al.* (1995) was $2d$. Their value is 17% greater than the present result; however, their wavelengths for mode A and mode B were similarly overstated, by 10% to 20%. The square cylinder wavelength quoted by Robichaux *et al.* (1999) was around 50% greater than the value reported here. The side length of the square cross-section was employed as the length scale for their study. This amplified the wavelength of each mode by a factor of approximately $\sqrt{2}$, as the vortex rollers in the wake of the square cylinder appeared to scale with the diagonal length of the square cross-section. Rescaling by this factor brings the spanwise wavelength of their mode S to within 10% of mode C in the present study. The time symmetry characteristics and topology of the mode C instability in the present study match the mode S instability of the square cylinder wake exactly. These characteristics will be discussed in the following sections.

4.3. *The mode A instability*

Numerical stability analysis of the straight cylinder by Barkley & Henderson (1996) predicts the spanwise wavelength of the mode A instability to be $3.96d$. The present study is in close agreement, as discussed previously. The fastest growing spanwise wavelength of the corresponding mode A instability for rings of aspect ratio $Ar = 20$, 40, 100 and 1000 is within 1.1% of the straight cylinder wavelength; however, as the aspect ratio decreases to $Ar = 5$, the wavelength increases to $4.5d$, 14.5% greater than that for the cylinder. Each of these rings became critically stable in the Reynolds-number range $188 \leqslant Re \leqslant 194$. The critical Reynolds number for rings with aspect ratio $Ar \geqslant 20$ is within 1.0% of the straight cylinder transition. The transition Reynolds number increases with decreasing aspect ratio until at $Ar = 5$ it occurs at a Reynolds number 3% higher than the transition for the straight cylinder. Visualizations of the streamwise vorticity of the perturbation fields of the dominant Floquet modes for these wakes (figure 13*a* for $Ar = 5$ and figure 14*a* for $Ar = 20$) reveal identical time-symmetry, and show a similar distribution of vorticity to those presented by Barkley & Henderson (1996) for the straight circular cylinder and Robichaux *et al.* (1999) for the square cylinder.

The wake of the $Ar = 5$ ring lacks the uniformity downstream that is observed in the circular cylinder wake, and the $Ar = 20$ ring wake, owing to the higher ring curvature casting the vortex cores radially outward as they convect downstream. It is still possible to compare the consistent sign of vorticity from one period to the next, and also the simple opposing sign vortical distribution for each pair of vortex street rollers, linking the perturbation field for the $Ar = 5$ ring with the mode A instability.

The perturbed wake maintained the same single-period ($1T$) symmetry as the mode A wake, and much of the perturbation streamwise vorticity is present within the vortex cores of the base flow vortex street. In each case, the vorticity is concentrated in vortex cores close to the cross-section, but dissipates $8d$ to $10d$ downstream.

4.4. *The mode B instability*

As with the mode A instability, a shorter-wavelength mode B instability was also predicted for all rings with aspect ratio $Ar \geqslant 5$. The critical Reynolds number for this instability is predicted at Reynolds numbers as high as $Re = 301$ for the ring with $Ar = 5$. The critical Reynolds number decreases to within 1.1% of the straight circular cylinder transition Reynolds number $Re = 258$ for rings with aspect ratio $Ar \geqslant 20$. The spanwise wavelength of the mode B instability lies within 2.5% of the straight circular cylinder wavelength for all rings with aspect ratios $Ar \geqslant 5$.

The Strouhal–Reynolds-number profiles for bluff rings found in experiment by Leweke & Provansal (1995) are not discontinuous through the mode B transition as observed for the straight circular cylinder wake (Williamson 1988*b*, 1996). Despite this, Leweke & Provansal (1995) do observe a change in gradient of the profiles in the Reynolds number range $255 < Re < 310$ consistent with the mode B transition regime highlighted in the present study. This gradient change suggests a gradual flow transition occurring in this Reynolds-number range, consistent with the nonlinear interaction of the saturated asymmetric wake following the mode A transition with the mode B instability.

It is proposed that the imposed periodicity of the ring geometry on the asymmetric wake structures imposes a gradual energy shift from Mode A wake structures to those corresponding to the Mode B wake. Thus, the transition to mode B is via a gradual impingement on the mode A structures globally, rather than the switching between

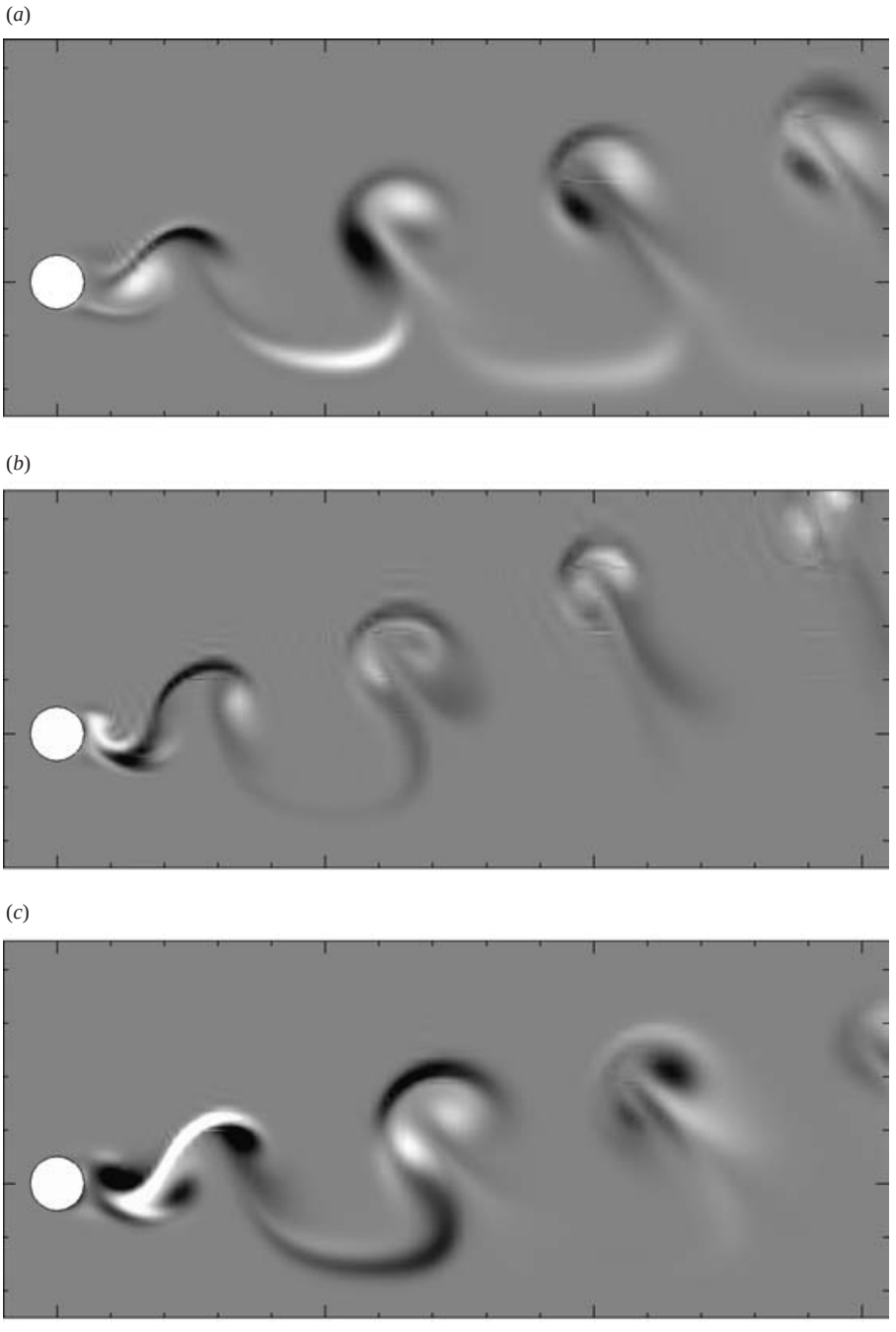

FIGURE 13. Streamwise vorticity of the perturbation field for the dominant azimuthal mode associated with the mode A, mode B and mode C transitions, with azimuthal wavelengths $3.93d$, $0.785d$ and $1.57d$, respectively, for a ring with aspect ratio $Ar = 5$. These transitions are shown in contour plots (*a*), (*b*) and (*c*), and are computed at Reynolds numbers of $Re = 200$, $Re = 305$ and $Re = 175$, respectively. Vorticity contours levels are arbitrarily chosen to elucidate the structure of the perturbation fields. Dark contours are negative, light contours are positive. Flow is from left to right, and the symmetry axis of the ring is located at the bottom of each frame.

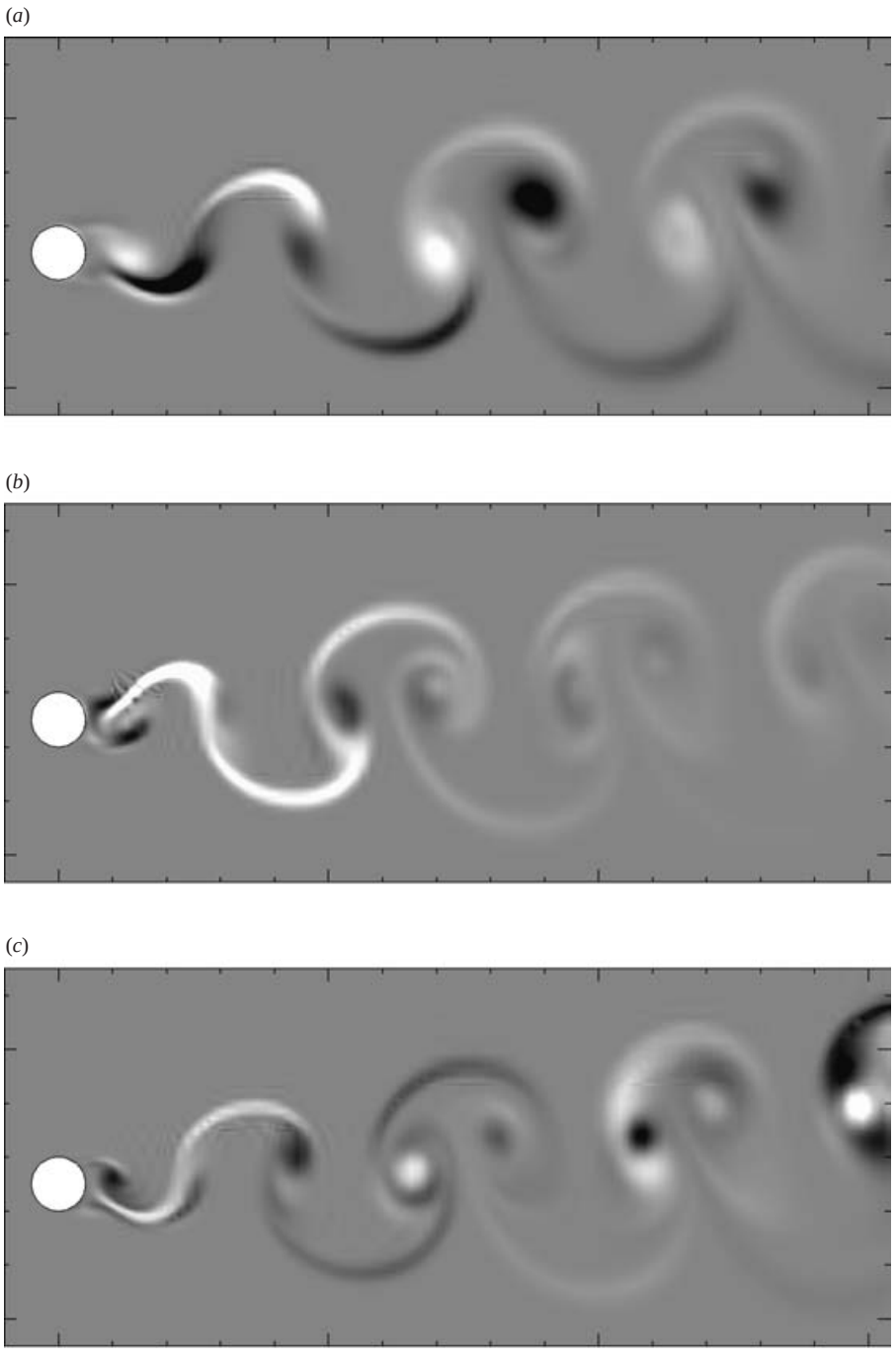

FIGURE 14. Streamwise vorticity of the perturbation field for the dominant azimuthal mode for each of the mode A, mode B and mode C transitions, with azimuthal wavelengths $3.93d$, $0.785d$ and $1.65d$, respectively, for a ring with aspect ratio $Ar = 20$. These transitions are shown in contour plots (a), (b) and (c), and are computed at Reynolds numbers of $Re = 200$, $Re = 265$ and $Re = 325$, respectively. Vorticity contours are arbitrarily chosen to elucidate the structure of the perturbation fields.

asymmetric modes or the local formation of different modes along the span seen for the straight circular cylinder (Williamson 1996; Henderson 1997).

The symmetry of the mode B instability is again of the $1T$ type, consistent with the previous studies of Robichaux *et al.* (1999), and Barkley & Henderson (1996). Figures 13(*b*) and 14(*b*) show plots of the streamwise vorticity of the mode B instability for rings with aspect ratios $Ar = 5$ and $Ar = 20$, respectively. Small portions of the plot in figures 13(*b*) and 14(*b*) appear slightly underresolved, owing to the interpolation of the computed vorticity over the mesh during post-processing. Despite the relatively high Reynolds number for the computation, and the higher spatial resolution required to resolve the perturbation field, the overall structure of the vorticity field is well defined, indicating good convergence.

4.5. *The mode C instability*

The intermediate-wavelength mode C instability has a maximum growth rate for spanwise wavelengths between $1.6d$ and $1.7d$. Figure 11 shows that this transition occurs at higher Reynolds numbers as the ring aspect ratio increases. For smaller aspect ratio rings, it in fact becomes the dominant transition mode. At $Ar = 5$, the mode C transition is the primary asymmetric vortex shedding mode; at $Ar = 10$, it is the secondary mode; and for rings with $Ar \geqslant 20$, it is the third mode to become unstable.

Streamwise vorticity plots of the perturbation field of the mode C instability are presented in figures 13(*c*) and 14(*c*) for aspect ratios $Ar = 5$ and $Ar = 20$, respectively. Note that the mode is characterized by a two-period ($2T$) symmetry, with the sign of the perturbation field vorticity alternating between each successive period of the base flow. The $2T$ temporal symmetry observed here is consistent with the square cylinder mode S observed by Robichaux *et al.* (1999), and may be observed as the reversal in sign of the vorticity distributed around each successive vortex core.

The decrease in aspect ratio also decreases the local symmetry between the fluid passing in and around the ring cross-section, and the resulting vortex shedding. It is this disruption of symmetry that appears to allow the mode C mode to become unstable, just as Zhang *et al.* (1995) found by causing a local disruption by inserting a tripwire close to the cylinder. In the absence of such a disruption, no mode at this spanwise wavelength is observed either through numerical stability analysis (Barkley & Henderson 1996; Noack & Eckelmann 1994*b*) or through experimental studies (Williamson 1988*b*).

As mentioned earlier, mode C has been observed in the wake of other geometries, such as the square cylinder (Robichaux *et al.* 1999). With regard to the stability of bluff-body wakes, the circular cylinder may be a special case, suppressing the mode C transition. The present study found no evidence of a mode C transition in the circular cylinder wake. Subcritical Floquet multipliers were observed corresponding to the projected wavelength of mode C; however, for increasing Reynolds number the multipliers remained absolutely stable ($\mu \ll 1$).

4.6. *The primary asymmetric transition of steady base flows for rings with* $0 \leqslant Ar < 4$

As shown, rings with $Ar \geqslant 4$ undergo a Hopf transition to unsteady flow prior to an asymmetric wake transition. Previous studies (Sheard *et al.* 2001) show that small rings ($Ar \leqslant 3$) undergo a transition to steady asymmetric flow prior to an unsteady flow transition. Further investigation revealed that this transition occurs at an aspect ratio of approximately $Ar = 3.9$.

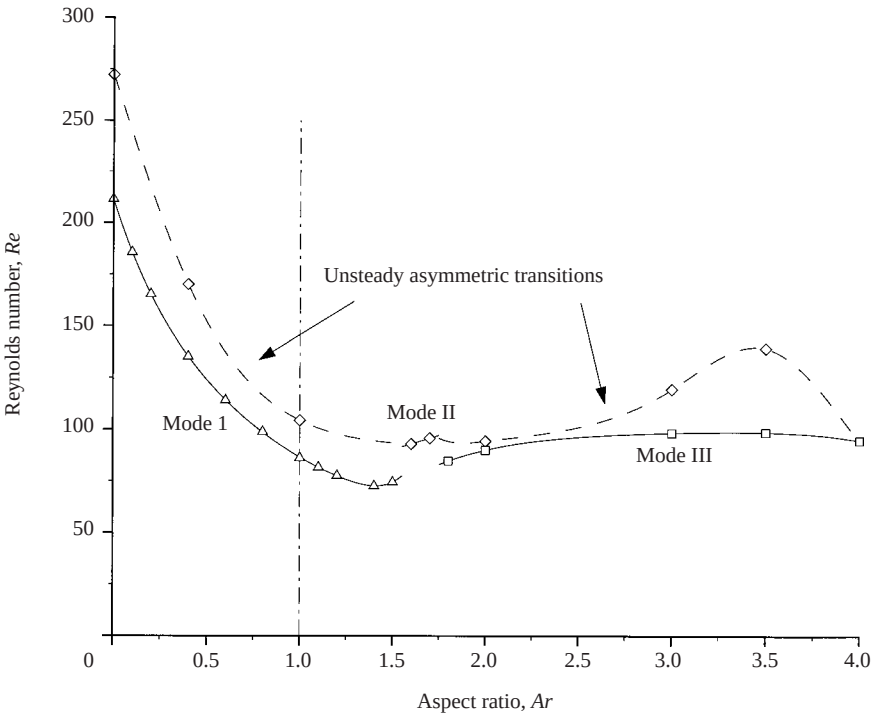

FIGURE 15. Asymmetric transition profile for small-aspect-ratio rings. The aspect ratio at which the axial hole appears is marked by the vertical dashed line. Solid lines represent the primary asymmetric transition modes, with triangles representing mode I, mode II represented by diamonds, and squares representing mode III. The dashed line approximates the secondary asymmetric Hopf transition profile, with points from asymmetric computations also indicated by diamonds.

The asymmetric transition profiles in figure 15 indicate the presence of three distinct transition modes over the aspect-ratio range $0 \leqslant Ar < 4$. These modes are here in after referred to as mode I, mode II and mode III. The perturbation field corresponding to the mode I instability over the aspect ratio range $0 \leqslant Ar \leqslant 1.5$ is analogous to the regular asymmetric transition mode of the sphere wake. For aspect ratios over the range $1.6 \leqslant Ar \leqslant 1.7$, an asymmetric Hopf transition mode dominates (mode II), and for the aspect-ratio range $1.8 \leqslant Ar < 4$, a regular asymmetric transition in the recirculating wake behind the ring cross-section (mode III) dominates.

Throughout the mode I aspect-ratio range, a rapid decrease in transition Reynolds number is experienced with increasing aspect ratio. The minimum critical Reynolds number reached is $Re = 72.6$ at $Ar = 1.4$. The steady decrease from $Re = 212$ at $Ar = 0$ (a sphere) indicates that the ring cross-section diameter, d, is not an appropriate length scale for rings of small aspect ratio, and a length scale based on the outer diameter of the ring $(D + d)$ would be more appropriate. Applying this length scale to the $Ar = 1.4$ ring, for example, would give a transition Reynolds number of $Re_{D+d} = 174$. This corresponds to a decrease of just 17.6% from the sphere transition Reynolds number at $Ar = 0$.

The azimuthal mode number of the mode III transition at $Ar = 2$ and $Ar = 3$ are $m = 1$ and $m = 2$, respectively. These transitions are classified on the one mode III transition branch, as the corresponding axisymmetric base flow scales on the ring cross-section, rather than the outer ring diameter (as per the mode I transition). Hence,

Aspect ratio range	Primary instability m	Secondary instability m
$0 \leqslant Ar \leqslant 2$	$m = 1$	$m = 1$
$3 \leqslant Ar \leqslant 3.5$	$m = 2$	$m = 2$

TABLE 3. Predicted azimuthal mode number of transition modes in the wake of rings with $Ar < 4$.

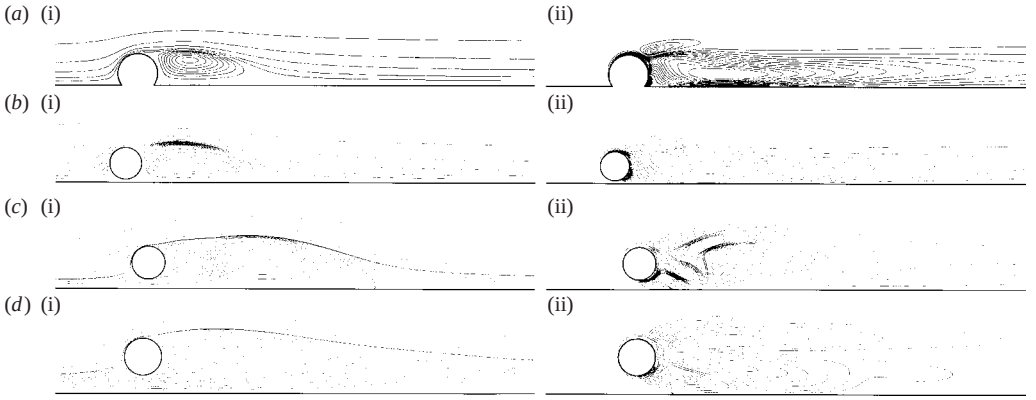

FIGURE 16. Pairs of (i) streamline plots and (ii) perturbation field streamwise vorticity contours at the asymmetric transition for rings with aspect ratio $Ar < 4$. The mode I transition is shown without the axial hole in (a), with aspect ratio $Ar = 0.6$ at $Re = 114$. The mode I transition with the axial hole is shown in (b), with $Ar = 1.2$ at $Re = 78$. The mode II transition is shown in (c), with $Ar = 1.6$ at $Re = 93$, and the mode III transition is shown in (d) with $Ar = 2$ at $Re = 90$. The axis is represented by a black line, and contour levels are chosen to highlight the flow structures (refer to figure 4).

the azimuthal wavelength of the mode III instability also scales with the cross-section diameter d, and the azimuthal mode number increases with aspect ratio to maintain the azimuthal wavelength. The important consideration is that the perturbation field of the dominant Floquet mode remains consistent over the mode III regime.

The dominant spanwise mode numbers at various aspect ratios are summarized in table 3. Both the primary asymmetric instability and the secondary instability are included.

Distinctions between the three transition modes become obvious when the perturbation fields of the transitions are analysed. Figure 16 shows both streamline plots of the axisymmetric base flows, and corresponding streamwise vorticity plots of the perturbation fields of each of the dominant Floquet modes in question.

4.6.1. *The mode I transition:* $0 \leqslant Ar \leqslant 1.5$

The variation of the critical Reynolds number for the mode I transition in figure 15 is continuous through $Ar = 1$. Thus, the emergence of the axial hole has no immediate effect on the transition, as the similarity in perturbation field distributions in figures 16(a) and 16(b) demonstrate. This continuity is a product of the similarity in structure of the large recirculating eddies in the near wakes of both small rings with a hole at the axis (figure 16b) and without a hole (figure 16a). For the sphere, the recirculation bubble becomes unstable to asymmetric perturbations, shifting radially from the axisymmetric state to form the classic double-threaded wake.

4.6.2. *The mode II transition:* $1.6 \leqslant Ar \leqslant 1.7$

The effect of the axial hole becomes apparent at aspect ratios $Ar \geqslant 1.6$, when the size of the hole is of the order of the cross-section of the ring. The corresponding transition mode is mode II mentioned previously, and visualized in figure 16(*c*). The base flow field is steady at this transition, and the perturbation field is also steady to about $1d$ downstream of the ring cross-section. Further downstream, a gentle oscillation of the perturbation field was observed, in the form of vorticity being shed from the tail of the wake. This oscillation had a Strouhal frequency $St = 0.00705$ at the critical Reynolds number for the transition.

The streamline plot of the base flow for mode II in figure 16(*c*) shows that the fluid passing through the hole travels a complex path downstream along the axis, recirculating back to the rear of the ring before being deflected around the axial recirculation bubble that resides $1 - 2d$ downstream. Thus, for this transition, the wake is too distended to permit the sphere transition mode to dominate, but there is also insufficient fluid passing through the axial hole of the torus to form the recirculating wake behind the ring cross-section necessary for mode III to dominate.

4.6.3. *The mode III transition:* $1.8 \leqslant Ar < 4$

The mode III transition arises when the recirculating vortex ring from the rear of the torus becomes unstable (see figure 16*d*).

4.7. *The asymmetric Hopf transitions for rings with* $0 \leqslant Ar < 4$

Thus far, the predicted primary asymmetric transition of the wake of bluff rings in the small-aspect-ratio range $0 \leqslant Ar < 4$ has been described (i.e. modes I, II and III). These wakes following the regular mode I and mode III transitions also experience a secondary asymmetric transition, leading to an unsteady wake. These primary and secondary transitions are similar to the primary and secondary transitions observed in the wake of a sphere (Johnson & Patel 1999). The sphere wake undergoes a primary regular asymmetric transition at $Re = 211$ followed by a secondary asymmetric Hopf transition at $Re \approx 270$.

4.7.1. *Secondary transitions in the mode I and mode III regimes*

The secondary transition following the mode I and mode III transitions is akin to the secondary transition of the sphere wake predicted by Natarajan & Acrivos (1993). They found similar transitions in the wakes of both spheres and disks: in both instances the perturbation fields of these secondary transition modes were characterized by the shedding of slanted alternating bands of positive and negative streamwise vorticity downstream from the rear of the bluff body.

A full linear stability analysis of the secondary transition in parameter space is yet to be performed. Critical-Reynolds-number profiles of the secondary transition are treated in a later section, as they could only be verified by means of asymmetric computations. This was due to a limitation of the stability analysis technique, whereby only the leading Floquet mode (i.e. the regular transition mode) could be resolved. As no regular asymmetric transition modes become unstable over the mode II range ($1.6 < Ar < 1.7$), the present Floquet stability analysis is applied to provide accurate predictions of the mode II Hopf transition Reynolds numbers and symmetry characteristics.

4.7.2. *Mode II: a spontaneous asymmetric Hopf transition*

In order to understand the nature of the mode II transition, a study of the stability of the $Ar = 1.6$ ring to this transition mode is presented. The axisymmetric base flow

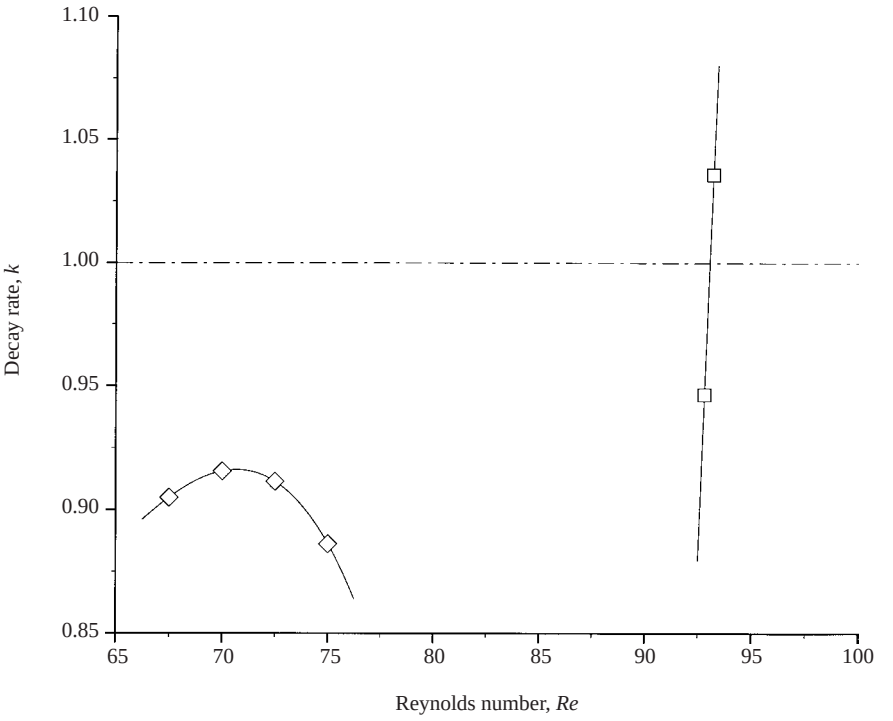

FIGURE 17. Leading asymmetric Floquet instability modes for the $Ar = 1.6$ ring with increasing Reynolds number. The absolutely stable real mode is represented by diamonds, and the imaginary Floquet mode (unstable for $Re \gtrsim 94$) is represented by squares. The neutral stability limit ($\mu = 1$) is indicated by the dashed line.

is absolutely stable to the primary Floquet mode (a real mode corresponding to a regular asymmetric transition of the wake). The highest Floquet multiplier for this mode is $\mu \approx 0.92$, for $Re \approx 70$, always below the neutral stability limit (i.e. $\mu < 1$).

A complex conjugate pair of Floquet multipliers (corresponding to an asymmetric Hopf transition) is the first Floquet mode to become unstable (i.e. $\mu > 1$). This mode is unstable for $Re \lesssim 94$, and is characterized by a periodic perturbation field. Profiles of the stability parameter space, showing these dominant Floquet modes, are provided in figure 17. A spontaneous Hopf transition from a steady axisymmetric wake flow to an unsteady asymmetric wake flow is therefore predicted for the mode II transition.

As discussed, aspect ratios $Ar \geqslant 4$ undergo an axisymmetric Hopf bifurcation prior to an asymmetric transition with increasing Reynolds number. In this case, the dominant azimuthal mode numbers elucidate the spanwise wavelength of the asymmetric vortex-shedding modes in terms of the ring cross-section diameter, d. Asymmetric computations presented in the next section are performed to capture the Hopf bifurcation of the steady asymmetric wakes in the mode I and mode III aspect ratio regime $0 \leqslant Ar \leqslant 1.5$ and $1.8 \leqslant Ar < 4$, respectively. Iso-surface plots are presented, verifying the predicted regular mode I transition and the mode A transition.

5. Results: asymmetric wake computations

This section details the determination of the profile of the critical Reynolds number of the asymmetric Hopf transition in the wake of bluff rings with aspect

ratios $Ar < 4.0$. Plots are also provided from asymmetric simulations validating the predictions of Floquet stability analysis.

5.1. *Capturing the unsteady transition in steady asymmetric wakes*

The critical Reynolds numbers for the unsteady asymmetric transition of bluff ring wakes with aspect ratios $0 \leqslant Ar < 4$ were approximated by interpolating the growth rates of unsteady transients in the wake around the Hopf transition Reynolds number for a zero growth rate. Hence, the transition Reynolds numbers are captured in a manner similar to the technique used to determine the critical Reynolds numbers for the axisymmetric Hopf transition for bluff rings with aspect ratio $Ar \geqslant 4$. The critical-Reynolds-number profile of the Hopf transition for small aspect ratios is shown in figure 15. Note the similarity between the measured Hopf transition at $Ar = 0$ of $Re_{S3} = 272.2$, and the accepted value for the secondary sphere wake transition $Re_{S3} \approx 272.5$.

The Hopf transition profile follows a trend similar to the regular asymmetric transition profile. Two points that have been made previously can be observed from the graph. One is the absence of a regular transition over the aspect ratio range $1.6 \leqslant Ar \leqslant 1.7$, as the mode II transition is a Hopf transition. The second is the intersection between the two transition profiles just prior to $Ar = 4.0$. This is the critical aspect ratio above which the wake flow fields exhibit unsteady behaviour prior to an asymmetric transition. Thus, the asymmetric transition for $Ar \gtrsim 4$ corresponds to an asymmetric vortex shedding mode.

5.2. *Asymmetric visualization of the predicted transition modes*

Although the full simulation of the various asymmetric transition modes presented in this paper is the subject of further work, we present here two examples of asymmetric wakes that agree with the predictions of the Floquet stability analysis. The wake of the $Ar = 0.6$ ring at $Re = 130$ is shown in figure 18. The mode I transition wake is observed, with asymmetric wake structures consistent with the wake behind the sphere (another mode I transition) following the regular asymmetric transition (Tomboulides & Orszag 2000; Thompson *et al.* 2001*a*). The double-threaded wake can be seen extending far downstream of the body. The predicted $m = 1$ azimuthal symmetry and the plane of symmetry along the axis are clearly evident, again consistent with the mode I sphere wake (Johnson & Patel 1999). The perturbation field presented in figure 16(*a*) illustrates the consistency between the perturbation field of the mode I transition, and the corresponding perturbation field of a sphere wake from the stability analysis of Natarajan & Acrivos (1993). Furthermore, the consistency of the iso-surface plot in figure 18 with the vortical structure of the asymmetric sphere wake following the regular asymmetric transition (Thompson *et al.* 2001*a*) show that the Floquet analysis applied in the present study correctly predicted the azimuthal symmetry and Reynolds-number range of the mode I transition.

The wake of the $Ar = 40$ ring at $Re = 200$ is shown in figure 19 to highlight the development of a mode A vortex-shedding wake, similar to that predicted behind the circular cylinder (Thompson *et al.* 1994, 1996). The azimuthal span is approximately $3.9d$, consistent with the mode A wake for the circular cylinder (Barkley & Henderson 1996). The spatio-temporal symmetry of the wake asymmetry, and the vorticity distribution observed here is also consistent with previous circular cylinder stability studies (Barkley & Henderson 1996), and experimental flow visualization (Williamson 1996).

FIGURE 18. The asymmetric wake of the $Ar = 0.6$ ring following the mode I transition at $Re = 130$. The ring is located at the top right-hand corner of the frame, and the flow direction is from the top right to the bottom left. Light and dark isosurfaces show negative and positive streamwise vorticity, respectively. Note the double-threaded wake structure, similar to the classic sphere wake.

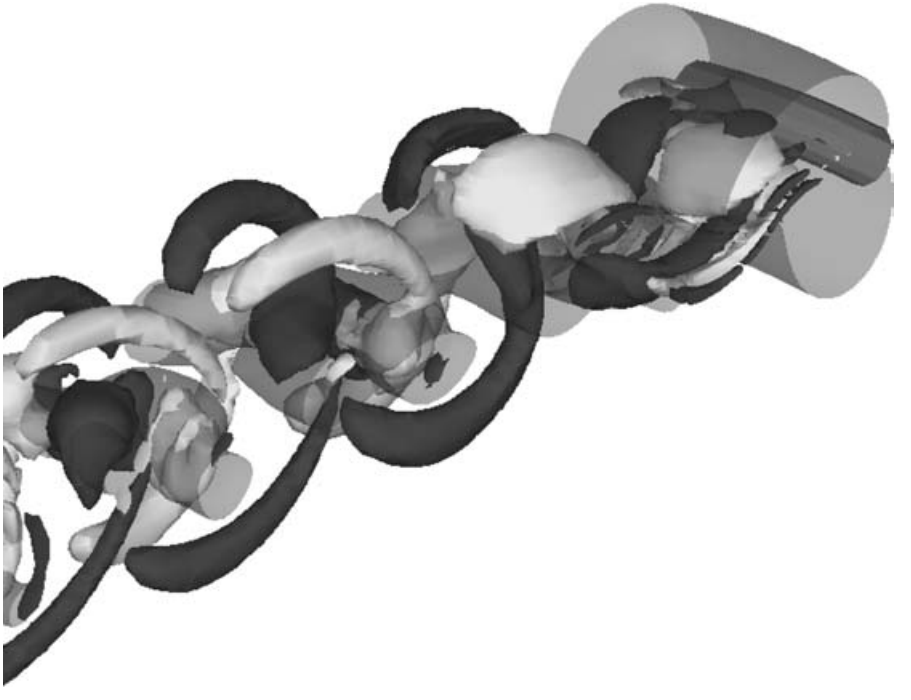

FIGURE 19. The asymmetric wake of the $Ar = 40$ ring following the mode A transition at $Re = 200$. Isosurfaces are shaded as in figure 18; however, a translucent isosurface is added, showing a pressure level of -0.01 units, to elucidate the vortex street. Note the counter-rotating streamwise vortex pairs in the braid region between the vortex cores. These structures are consistent with the mode A wake structures observed in the wake of the circular cylinder. The simulated azimuthal span is approximately $3.9d$.

6. Conclusions

Results have been presented from both axisymmetric direct numerical simulations, and linear Floquet stability analysis of the wakes of bluff rings. Strouhal–Reynolds-number profiles have been presented for a wide range of aspect-ratios, as have critical Reynolds numbers pertaining to the transitions to separated flow, unsteady flow and asymmetry in the wake. Furthermore, asymmetric simulations have ascertained the approximate transition to unsteady flow for those rings that exhibit steady asymmetric flow structures prior to a transition to unsteady flow. Floquet analysis has allowed us to make further predictions with respect to the asymmetric wake structures based on the perturbation fields obtained, and comparison with existing work.

The single-parameter torus geometry has proved to be an excellent geometry for the study of a plethora of wake flow transitions. The simplicity in modelling the torus numerically makes it an attractive geometry for the study of geometric effects on bluff-body flow.

Studying the torus has enabled us to observe why the behaviour of the wake of the sphere is so different to the wake of the straight circular cylinder. We have identified which wake features and flow structures correspond to the various transitions that are predicted. The full parameter space of both axisymmetric and asymmetric flow-transition Reynolds numbers has been mapped as a function of aspect ratio. This parameter study, coupled with the presented streamline plots of the wakes for various aspect ratios and flow transitions, provides a significant contribution to the understanding of the effect a geometry has on both the order and types of transition likely to occur in its wake prior to turbulent flow.

Rings with $Ar < 3.9$ are predicted to undergo a transition to asymmetric flow prior to a transition to unsteady flow. Three distinct transition modes have been identified and characterized in this aspect-ratio range. These transitions, modes I, II and III, occur over aspect-ratio ranges $Ar < 1.6$, $1.6 \leqslant Ar \leqslant 1.7$ and $1.7 < Ar < 3.9$, respectively. The regular bifurcation to asymmetry in the wake of the sphere is an example of a mode I transition.

Rings of intermediate aspect ratio, $3.9 \lesssim Ar \lesssim 8$, are predicted to undergo a asymmetric mode C transition of the axisymmetric vortex-shedding wake. This mode does not occur in an unperturbed circular cylinder wake, or a sphere or disk wake. Rings of aspect ratios $Ar \gtrsim 8$ were shown to undergo an initial transition to asymmetric vortex shedding analogous to the mode A shedding from the straight circular cylinder. A summary of the asymmetric transition modes predicted for the bluff ring system is presented in table 4.

Investigation into rings of aspect ratios $0 \leqslant Ar < 1.6$ showed that they scaled with a Reynolds number based on the overall ring diameter $D + d$, rather than the ring cross-section diameter, d. This was evident from the decrease in transition Reynolds numbers for flow separation, asymmetric flow and unsteady flow.

Asymmetric flow simulations permitted the verification of the unsteady transition of ring wakes for $0 \leqslant Ar < 3.9$. Visualization of the saturated wakes following both the mode I transition of the wake of a ring with an aspect ratio $Ar = 0.6$, and the mode A transition of a ring with aspect ratio $Ar = 40$ are provided. These aspect ratios were chosen because of their similarity to the limiting sphere and circular cylinder geometries, respectively. The computed asymmetric wake structures agree with the predictions of the Floquet stability analysis pertaining to the symmetry of these modes, and pave the way for a thorough study of the asymmetric bluff ring parameter space, to be the subject of a future publication.

Ar range	Asymmetric transition mode		
	Primary transition	Secondary transition	Tertiary transition
$0 \leqslant Ar < 1.6$	Regular mode I $m = 1$ symmetry	Hopf mode I $m = 1$ symmetry	
$1.6 \leqslant Ar \leqslant 1.7$	Hopf mode II $m = 1$ symmetry		
$1.7 < Ar \lesssim 3.9$	Regular mode III $4.7d < \lambda_d < 7.9d$	Hopf mode III $4.7d < \lambda_d < 7.9d$	
$3.9 \lesssim Ar \lesssim 8$	Mode C $\lambda_d \approx 1.7d$	Mode A $\lambda_d \approx 4.0d$	Mode B $\lambda_d \approx 0.8d$
$8 \lesssim Ar \lesssim 13$	Mode A $\lambda_d \approx 4.0d$	Mode C $\lambda_d \approx 1.7d$	Mode B $\lambda_d \approx 0.8d$
$13 \lesssim Ar < \infty$	Mode A $\lambda_d \approx 4.0d$	Mode B $\lambda_d \approx 0.8d$	Mode C $\lambda_d \approx 1.7d$

TABLE 4. Summary of the asymmetric transition modes for bluff ring wakes.

The authors wish to thank the Victorian Partnership for Advanced Computing (VPAC) and the Australian Partnership for advanced computing (APAC) for providing the necessary computational resources required to complete this investigation. G. J. S. gratefully acknowledges the financial backing of the Australian Postgraduate Award research scholarship.

REFERENCES

BARKLEY, D. & HENDERSON, R. 1996 Three-dimensional Floquet stability analysis of the wake of a circular cylinder. *J. Fluid Mech.* **322**, 215–241.

BEARMAN, P. & TAKAMOTO, M. 1988 Vortex shedding behind rings and disks. *Fluid Dyn. Res.* **3**, 214.

DUŠEK, J., FRAUNIÉ, P. & LE GAL, P. 1994 A numerical and theoretical study of the first Hopf bifurcation in a cylinder wake. *J. Fluid Mech.* **264**, 59–80.

GHIDERSA, B. & DUŠEK, J. 2000 Breaking of axisymmetry and onset of unsteadiness in the wake of a sphere. *J. Fluid Mech.* **423**, 33–69.

HENDERSON, R. 1997 Nonlinear dynamics and pattern formation in turbulent wake transition. *J. Fluid Mech.* **352**, 65–112.

HOURIGAN, K., REICHL, P. & THOMPSON, M. 2002 Unsteady separated flow near a free surface. In *Invited Keynote Lecture, IUTAM Symposium on Unsteady Separated Flows, Toulouse, France.*

HOURIGAN, K., THOMPSON, M. & TAN, B. 2001 Self-sustained oscillations in flows around long flat plates. *J. Fluids Struct.* **15**, 387–398.

JOHNSON, T. & PATEL, V. 1999 Flow past a sphere up to a Reynolds number of 300. *J. Fluid Mech.* **378**, 19–70.

KARNIADAKIS, G. 1990 Spectral element – Fourier methods for incompressible turbulent flows. *Comput. Methods Appl. Mech. Engng* **80**, 367–380.

LEWEKE, T. & PROVANSAL, M. 1995 The flow behind rings: bluff body wakes without end effects. *J. Fluid Mech.* **288**, 265–310.

LEWEKE, T. & WILLIAMSON, C. 1998 Cooperative elliptic instability of a vortex pair. *J. Fluid Mech.* **360**, 85–119.

MAGARVEY, R. & BISHOP, R. 1961*a* Transition ranges for three-dimensional wakes. *Can. J. Phys.* **39**, 1418–1422.

MAGARVEY, R. & BISHOP, R. 1961*b* Wakes in liquid–liquid systems. *Phys. Fluids* **4**, 800–805.

MAGARVEY, R. & MACLATCHY, C. 1965 Vortices in sphere wakes. *Can. J. Phys.* **43**, 1649–1656.

MILLS, R., SHERIDAN, J. & HOURIGAN, K. 2002 Response of base suction and vortex shedding from rectangular prisms to transverse forcing. *J. Fluid Mech.* **461**, 25–49.

Mills, R., Sheridan, J. & Hourigan, K. 2003 Particle image velocimetry and visualization of natural and forced flow around rectangular cylinders. *J. Fluid Mech.* **478**, 299–323.

Mittal, R. 1999*a* A Fourier–Chebyshev spectral collocation method for simulating flow past spheres and spheroids. *Intl J. Numer. Fluids* **30**, 921–937.

Mittal, R. 1999*b* Planar symmetry in the unsteady wake of a sphere. *AIAA J.* **37**, 388–390.

Mittal, R. & Balachandar, S. 1995 Generation of streamwise vortical structures in bluff body wakes. *Phys. Rev. Lett.* **75**, 1300–1303.

Monson, D. 1983 The effect of transverse curvature on the drag and vortex shedding of elongated bluff bodies at low Reynolds number. *Trans. ASME* I: *J. Fluids Engng* **105**, 308–317.

Natarajan, R. & Acrivos, A. 1993 The instability of the steady flow past spheres and disks. *J. Fluid Mech.* **254**, 323–344.

Noack, B. & Eckelmann, H. 1994*a* A global stability analysis of the steady and periodic cylinder wake. *J. Fluid Mech.* **270**, 297–330.

Noack, B. & Eckelmann, H. 1994*b* A low-dimensional Galerkin method for the three-dimensional flow around a circular cylinder. *Phys. Fluids* **6**, 124–143.

Ormières, D. & Provansal, M. 1999 Transition to turbulence in the wake of a sphere. *Phys. Rev. Lett.* **83**, 80–83.

Patera, A. 1984 A spectral element method for fluid dynamics: laminar flow in a channel expansion. *J. Comput. Phys.* **54**, 468–488.

Robichaux, J., Balachandar, S. & Vanka, S. 1999 Three-dimensional Floquet instability of the wake of a square cylinder. *Phys. Fluids* **11**, 560–578.

Roshko, A. 1953 On the development of turbulent wakes from vortex streets. *NACA TN* , p. 2913.

Sheard, G., Thompson, M. & Hourigan, K. 2001 A numerical study of bluff ring wake stability. In *Proc. 14th Australasian Fluid Mech. Conf. Department of Mechanical Engineering, University of Adelaide.*

Sheard, G., Thompson, M. & Hourigan, K. 2002 On axisymmetric bluff body wakes: three-dimensional wake structures and transition criticality of the torus. In *Proc. 3rd Conf. on Bluff Body Wakes and Vortex Induced Vibrations, Port Douglas, Australia.*

Thompson, M., Hourigan, K. & Sheridan, J. 1994 Three-dimensional instabilities in the wake of a circular cylinder. In *Proc. Intl Colloquium on Jets, Wakes and Shear Layers* (ed. K. Hourigan). CSIRO, Melbourne.

Thompson, M., Hourigan, K. & Sheridan, J. 1996 Three-dimensional instabilities in the wake of a circular cylinder. *Expl Therm. Fluid Sci.* **12**, 190–196.

Thompson, M., Leweke, T. & Provansal, M. 2001*a* Kinematics and dynamics of sphere wake transition. *J. Fluids Struct.* **15**, 575–585.

Thompson, M., Leweke, T. & Williamson, C. 2001*b* The physical mechanism of transition in bluff body wakes. *J. Fluids Struct.* **15**, 607–616.

Tomboulides, A. & Orszag, S. 2000 Numerical investigation of transitional and weak turbulent flow past a sphere. *J. Fluid Mech.* **416**, 45–73.

Tomboulides, A., Orszag, S. & Karniadakis, G. 1993 Direct and large-eddy simulation of the flow past a sphere. In *Proc. 2nd ICTME*.

Williamson, C. 1988*a* Defining a universal and continuous Strouhal–Reynolds number relationship for the laminar vortex shedding of a circular cylinder. *Phys. Fluids* **31**, 2742–2744.

Williamson, C. 1988*b* The existence of two stages in the transition to three-dimensionality of a cylinder wake. *Phys. Fluids* **31**, 3165–3168.

Williamson, C. 1989 Oblique and parallel mode of vortex shedding in the wake of a circular cylinder at low Reynolds numbers. *J. Fluid Mech.* **206**, 579–627.

Williamson, C. 1996 Three-dimensional wake transition. *J. Fluid Mech.* **328**, 345–407.

Zhang, H., Noack, B., König, M. & Eckelmann, H. 1995 On the transition of the circular cylinder wake. *Phys. Fluids* **7**, 779–793.